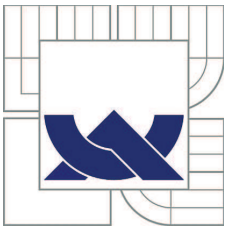

VYSOKÉ UČENÍ TECHNICKÉ V BRNĚ
BRNO UNIVERSITY OF TECHNOLOGY

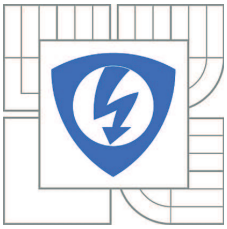

FAKULTA ELEKTROTECHNIKY A KOMUNIKAČNÍCH TECHNOLOGII
ÚSTAV BIOMEDICÍNSKÉHO INŽENÝRSTVÍ

THE FACULTY OF ELECTRICAL ENGINEERING AND COMMUNICATION
DEPARTMENT OF BIOMEDICAL ENGINEERING

IMAGE RECONSTRUCTION FROM NON-CARTESIAN K-SPACE DATA ACQUIRED BY ULTRA-SHORT ECHO-TIME AND FAST MR IMAGING METHODS

REKONSTRUKCE OBRAZU Z NEKARTÉZSKÝCH K-PROSTOROVÝCH DAT ZÍSKANÝCH METODAMI MAGNETICKOREZONANČNÍHO ZOBRAZOVÁNÍ S ULTRAKRÁTKÝM ECHO-ČASEM A METODAMI RYCHLÉHO MR ZOBRAZOVÁNÍ

BAKALÁŘSKÁ PRÁCE
BACHELOR'S THESIS

AUTOR PRÁCE
AUTHOR

TOMÁŠ PŠORN

VEDOUCÍ PRÁCE
SUPERVISOR

Ing. ZENON STARČUK, CSc.

BRNO 2015

BRNO UNIVERSITY OF TECHNOLOGY

Faculty of Electrical Engineering and Communication

Department of Biomedical Engineering

Bachelor thesis

Bachelor's study field

Biomedical Technology and Bioinformatics

Student: Tomáš Pšorn ***ID:*** 155599

Year of study: 3 ***Academic year:*** 2014/15

TITLE OF THESIS:

Image reconstruction from non-Cartesian k-space data acquired by ultra-short echo-time and fast MR imaging methods

INSTRUCTION:

1) Review measurement and image reconstruction methods for ultrashort echo-time MR imaging with a nonrectangular k-space grid, and experimental methods for k-trajectory measurement. Focus on universally applicable methods and utilizability of redundancy in oversampled areas and, optionally, of prior knowledge. 2) Prepare pulse sequences for the acquisition of experimental data with a Cartesian and non-Cartesian grid on a MR scanner at ÚPT, carry out simple phantom measurements. Prepare analogous pulse sequences for simulation (NMRScopeB) and acquire model data. 3) Develop suitable image calculation methods, verify with data of task 2. Evaluate the methods from the point of view of artifacts, SNR, computational complexity, sensitivity to experimental conditions; verify k-trajectories experimentally. 4) Present practical results, compare with rectangular-grid measurements. 5) Evaluate the results achieved, analyze weaknesses and improvement possibilities.

REFERENCE:

[1] BERNSTEIN MA et. al. “Handbook of MRI Pulse Sequences”, Elsevier Academic Press, 2004.
[2] LEVITT MH. “Spin Dynamics: Basics of Nuclear Magnetic Resonance”, John Wiley & Sons, 2008.

Assigment deadline: 9. 2. 2015 ***Submission deadline:*** 29.5.2015

Head of thesis: Ing. Zenon Starčuk, CSc.

Consultant:

prof. Ing. Ivo Provazník, Ph.D.

Subject Council chairman

WARNING:

Abstrakt
Cílem této práce je teoretické seznámení s technikou rekonstrukce MRI obrazu nasnímaného na nekartézský rastr (např. radiální, spirální, atd.). Část práce se zabývá metodami měření přesnosti gradientního systému, která je pro snímání na nekartézský rastr obzvlášť důležitá. V praktické části je představen 4.7 T a 9.4 MRI systém na Ústavu přístrojové techniky AV ČR, v. v. i.. Systémy jsou použity pro nasnímání modelových dat s použitím existujících pulsních sekvencí.

Summary
The aim of this thesis is to handle theoretically the technique of MRI image reconstruction from non-Cartesian data such as radial, spiral, etc. Since later progress of this thesis will include actual measuring of non-Cartesian data, which is prone to the gradient infidelity, methods for measuring a performance of the gradient system will also be discussed. In practical part I will present the way the 4.7 T and 9.4 T MRI systems of the Institute of Scientific Instruments of the ASCR, v. v. i., works and use the existing pulse sequences to measure some model data.

Klíčová slova
MRI, k-prostor, MRI simulace, ne-Kartzská vzorkovací mřížka, proměnná hustota vzorkování, 2D interpolace, FFT, UTE, spirální EPI, měření k-trajektorie, digitální filtrace, skupinové zpoždění, náhodné vzorkování, 2D přemřížkování, SNR, obrazové artefakty, rozptilová funkce

Keywords
MRI, k-space, MRI simulation, non-Cartesian sampling grid, variable sampling density, 2D interpolation, FFT, UTE, spiral EPI, k-trajectory measurement, digital filtration, group delay, randomized sampling, 2D gridding, SNR, image artifacts, point spread function

PŠORN, T.*Image reconstruction from non-Cartesian k-space data acquired by ultra-short echo-time and fast MR imaging methods.* Brno: Vysoké učení technické v Brně, Fakulta elektrotechniky a komunikačních technologii, 2015. 57 s. Vedoucí diplomové práce Ing. Zenon Starčuk, CSc..

Prohlašuji, že svoji bakalářskou práci na téma Rekonstrukce obrazu z nekartézských k-prostorových dat získaných metodami magnetickorezonančního zobrazování s ultrakrátkým echo-časem a metodami rychlého MR zobrazování jsem zpracoval samostatně pod vedením vedoucího bakalářské práce a s použitím odborné literatury a dalších informačních zdrojů, které jsou všechny citovány v práci a uvedeny v seznamu literatury na konci práce. Jako autor uvedené bakalářské práce dále prohlašuji, že v souvislosti s vytvořeníním této práce jsem neporušil autorská práva třetích osob, zejména jsem nezasáhl nedovoleným způsobem do cizích autorských práv osobnostních a jsem si plně vědom následků porušení ustanovení § 11 a následují cích autorského zákona č. 121/2000 Sb., včetně možných trestněprávních důsledků vyplývajících z ustanovení § 152 trestního zákona č. 140/1961 Sb.

Tomáš Pšorn

I would like to thank my supervisor Ing. Zenon Starčuk CSc. for all his time, advices, patience and for motivating me to allways chose the difficult way. I would also like to thank all the staff on NMR research group of the ISI, who helped me, little by little, to go trough all the difficulties of the NMR, I've encountered. And last, but not least to my family for all their support.

Tomáš Pšorn

Contents

Introduction

The aim of this thesis is to handle theoretically the technique of MRI image reconstruction from non-Cartesian data such as radial, spiral. Since later progress of this thesis will include actual measurment of non-Cartesian data, which is prone to gradient infidelity, methods for measuring the performance of the gradient system will also be discussed. In practical part, the functionality of 4.7 T and 9.4 T MRI system of the Institute of Scientific Instruments of the ASCR, v. v. i., works and use the existing pulse sequence to measure some model data.

In chapter 1. history of NMR and MRI is briefly introduced. The basic principles of MRI are explained in order to be easy to understood in chapter 2.

Image reconstruction methods are discused in chapter 3. First of all, gridding is presented, since it is nowadays probably the most widely used approach for image reconstruction from non-uniformly sampled data. An interesting approach is to use lookup table for accelerating the reconstruction algorithm used. Then there is a description of the non-uniform fast Fourier transform, which generalizes the DFT, so it's not so computationally demanding when processing non-uniform data.

The fidelity of an image reconstructed from a non-Cartesian data is sensitive to the k-trajectory fidelity in particular, so it's relevant to pay attention to this fact. Therefore, some methods for measuring of the gradient system performance are described in chapter 4.

Chapters 5 and 6 provide some basic insight among methods of fast MRI imaging, such as UTE, EPI and Spiral. Their technical details will be discussed and applications mentioned.

The actual implementation of reconstruiction method and it's incorporation into the final software solution is explained. Further on testing on SW phantoms with both radial and spiral k-space trajectory is performed and discussion about results is given in chapter 7.

Measurement with UTE pulse sequences and its results are discussed in chapter 8

1. History of NMR and MRI

The history of Nuclear Magnetic Resonance began to be written in 1922, when Stern-Gerlach experiment was demonstrated for the first time [1]. It was conducted by Otto Stern and Walter Gerlach (both German physicists). In this experiment a beam of electrically neutral atoms is passing through inhomogeneous magnetic field and afterwards their distribution on the detector is observed. In the result, the quantum nature of intrinsic magnetic moment of each particle was demonstrated (also the influence of the measurement of a quantum system). The true breakthrough was, however, denoted by Isidor Rabi, who discovered the phenomenon of nuclear magnetic resonance in 1940's. He improved the Stern-Gerlach experiment to be more precise, so he was able to detect and measure the magnetic moment of the nuclei.

Edward M. Purcell in 1945 and Felix Bloch in 1946 independently of each other, by using different experiments and different samples, observed nuclear magnetic resonance for the first time. Together they received Nobel Prize. Erwin Hahn in 1949 shown, that instead of continuous wave excitation a short RF pulse can be used. He also shown, the so-called pulse can add some more information into measured signal [2].

Figure 1.1: Nobel prize laureates, from the left: Otto Stern (physics, 1943), Isidor I. Rabi (physics, 1944), Felix Bloch and Edward M. Purcell (physics, 1952)

In 1950's NMR was brought to the field of chemistry. Herbert S. Gutowsky *et al.* was conducting a number of experiments NMR spectroscopy [3]. He developed a method for identification and characterization of chemical compounds based on spin-spin coupling effect. Albert Overhauser predicted the Nuclear Overhauser in 1953, which was verified later and enabled the study of 3D molecular structure. Another important discovery was made by Paul Lauterbur in 1957, he developed a method of ^{13}C NMR spectroscopy. It was one of the first successful attempts for obtaining a spectrum of atom with such a low natural abundance (1.1%).

A significant breakthrough regarding scanning efficiency was the discovery of FT-NMR spectroscopy. In 1957 Richard E. Norberg and Irving J. Lowe showed, that applying Fourier transform on FID signal following an RF excitation yields the same spectrum as CW-NMR (continuous wave). However, their method of spectrum measurement was dramatically less time consuming. In 1966 Richard Ernst and Weston Anderson introduced the first FT-NMR spectrometer.

Another significant progress of NMR spectroscopy was the introduction of 2D NMR spectroscopy by Jean Jeener in 1971 and its further realization by Richard Ernst in 1975. It enabled researchers to access yet non-accessible information about the structure of molecules and about intramolecular interactions.

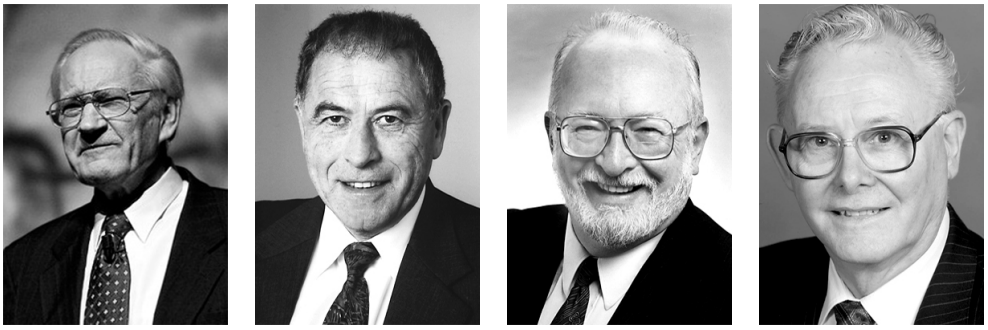

Figure 1.2: Nobel prize laureates, from the left: Richard R. Ernst (chemistry, 1991), Kurt Wüthrich (chemistry, 2002), Paul C. Lauterbur and Peter Mansfield (physiology or medicine, 2003)

The history of MRI begins with the research of two independently working scientists. Both Paul Lauterbur and Peter Mansfield used magnetic field gradients to encode spatial information into the NMR signal in 1974. One year later, Richard Ernst used Fourier transform to exploit frequency and spatial information to produce 2D image. These methods started a boom in MRI pretty soon imaging of different parts of human body became possible. In 1977 Damadian performed the first whole body MRI scan. In late 1980's MRI became popular diagnostic method for diagnosis of various diseases. Another discovery denoted by Mansfield, the echo planar imaging (EPI), accelerated image acquisition time (orders of milliseconds) and thus brought significant robustness towards motion artifacts. It improved cardiac and angiographic images, and enabled mapping of cerebral activity via the fMRI method.

In 1985 Kurt Wütrich developed a method to determine the structures and dynamics of biological macromolecules and their complexes in solution and with atomic resolution. He published its results in 1985 and received the Nobel Prize in Chemistry in 2002.

The progress of NMR, MRI and NMR spectroscopy was always profiting from discoveries of other fields of science and engineering, and vice versa. Great benefit for MRI was, for example, the application of superconductivity into electromagnet design which improved magnetic field homogeneity, or the massive progress in microcomputer design, which enabled processing of large collections of data. On the other hand, MRI moved the possibilities of medical diagnostic and research notably forward, whereas NMR spectroscopy provides information about structure and interaction of atoms and molecules, which are non-accessible by any other chemical methods.

2. Magnetic Resonance Imaging principles

The MRI is a very sophisticated and complex imaging modality. In this chapter a brief description of MRI process phenomena is given. It is essential to understand them to grasp the idea of the whole thesis.

2.1. Spin

ig

Spin, as well as mass, electric charge and magnetism, is an important property of atomic nuclei [4]. It is a rather special form of angular momentum, because is not a consequence of rotational movement. Spin is considered to be an intrinsic property of the particle itself. It's identified by spin quantum number S (often called spin). The value of spin is always given by an integer multiple of $\frac{1}{2}$ i.e. it's quantized. Protons, neutrons and electrons have the spin value of $\frac{1}{2}$. The spin quantum number of nucleus, denoted by I, is given by combining spins of protons and neutrons with respect to certain rules. The total nuclear angular momentum vector $\vec{L}$ can be determined using (2.1). Here $\hbar$ stands for the reduced Planck constant ($1.054 \times 10^{-34} Js$).

$$\vec{L} = \hbar\sqrt{I\left(I + \frac{1}{2}\right)} \tag{2.1}$$

The orientation of nuclear angular momenta is random under normal conditions. From now on the nuclear angular momentum will be denoted as nuclear spin or spin.

2.2. Precession

Another intrinsic property of atomic particles and by extension of atomic nuclei is a magnetic moment $\vec{\mu}$. The idea of NMR is rather dependent on the way nuclear magnetic momenta interact with magnetic field intensity $\vec{B}$ of NMR system. The presence of external magnetic field leads to precession movement of nuclear magnetic momenta.
As well as the spin, the nuclear magnetic moment is intrinstic property of protons, not a direct consequence of motion of electric charge. Spin and nuclear magnetic moment vectors are proportional (2.2). The proportionality coeficient γ is called gyromagnetic ratio (magnetogyric ratio). Their orientation is, in macroscopic scope, either paralel (nuclei with $\gamma > 0$), or antiparalel (nuclei with $\gamma < 0$).

$$\vec{\mu} = \gamma\vec{L} \tag{2.2}$$

Let us now apply the external magnetic field $\vec{B}$. The dot product (2.3) of $\vec{\mu}$ and $\vec{B}$ yelds the magnetic energy of nucleus resulting from magnetic interaction.

$$E_{mag} = -\vec{\mu} \cdot \vec{B} \tag{2.3}$$

However the cross product (2.4) of $\vec{\mu}$ and $\vec{B}$ yelds the vector of torque $\vec{N}$ acting on nuclear magnetic moment (nuclear torque).

$$\vec{N} = \vec{\mu} \times \vec{B} \tag{2.4}$$

And since the relation between nuclear torque and spin is given by (2.5).

$$\vec{N} = \frac{d\vec{L}}{dt} \tag{2.5}$$

By substituing in (2.4), the simplified Bloch equation (2.6) can be derived. It describes the way nuclear magnetic momenta interact with magnetic field. The movement expressed as a change of nuclear magnetic moment over the time is called precession.

$$\frac{d\vec{\mu}}{dt} = \gamma\vec{\mu} \times \vec{B} \tag{2.6}$$

The module of nuclear magnetic moment $|\vec{\mu}|$ remains constant, as well as the angle between $\vec{\mu}$ and B_0. Let the z' axis of the frame of reference of the MRI system to be parallel to the external magnetic field denoted by B_0. The position of nuclear magnetic moment vector as a function of time is derived in [6] as a solution of (2.6), the movement consequent to this function is called precession. Eq. (2.7) decomposes this function to individual cartesian axes x',y',z'.

$$\begin{aligned} \mu_{x'}(t) &= \mu_{x'}(0)cos\omega_0 t + \mu_{y'}(0)sin\omega_0 t \\ \mu_{y'}(t) &= \mu_{y'}(0)cos\omega_0 t - \mu_{x'}(0)sin\omega_0 t \\ \mu_{z'}(t) &= \mu_{z'}(0) \end{aligned} \tag{2.7}$$

Angular frequency ω_0 in (2.7) is called Larmor frequency. It's value is generaly on the intensity of applied magnetic field and gyromagnetic ratio via rather familiar eq. (2.8).

$$\omega = -\gamma B \tag{2.8}$$

For imaging of macroscopic objects, rather than describing magnetic momenta of isolated nuclei, it is suitable to use a sumation of nuclear magnetic momenta over volume, which results in a vector called local nett magnetization $\vec{M}_0$.

$$\vec{M}_0 = \frac{1}{V}\sum_{i}^{n}\vec{\mu}_i \tag{2.9}$$

Related volume unit is then refered to as the voxel. Size of voxel is to be chosen large enough for n to be high enough to allow neglecting quantum phenomena, but small enough to ensure almost homogenous B_0 in all the volume. Since the B_0 is considered homogenous within the voxel, then pack of spins contained in the voxel precesses with equal ω_0. Such pack of spins is called isochromate. Convention is to separate longitudinal $M_\parallel$ and transversal $M_\perp$ component of M.

$$M_\parallel = M_z \tag{2.10}$$

$$M_\perp = M_x\hat{x} + M_y\hat{y} \tag{2.11}$$

In (2.11) $\hat{x}$ and $\hat{y}$ denote unit vectors in direction of x and y axis. It is to be mentioned at this point, that all nuclear spins of each voxel precess with the same frequency (2.8), but they differ in phase and thus in direction. Since n is sufficiently large, the transverse components of nuclear spins are approximately canceled out. Consequently the transverse component of net magnetization $M_\perp$ is of zero magnitude.

It is sufficient for the needs of this thesis to operate with net magnetization vector, thus description of following phenomena will disregard remarks about interactions of individual spins in most cases. Basic form of Bloch equation for net magnetization vector (2.12) is obtained by combining (2.6) and (2.9).

$$\frac{d\vec{M}}{dt} = \gamma\vec{M} \times \vec{B} \tag{2.12}$$

Eq. (2.12) can be further separated into longitudinal and transversal part.

$$\frac{d\vec{M}_\parallel}{dt} = 0 \tag{2.13}$$

$$\frac{d\vec{M}_\perp}{dt} = \gamma\vec{M}_\perp \times \vec{B} \tag{2.14}$$

Equations (2.13) and (2.14) don't take into account interactions of nuclear spins with their surrounding. Additional terms will be appended in following chapter.

2.3. Frames of reference

In later description of MRI phenomena, certain manipulation with nuclear magnetic moment is performed by applying radiofrequency magnetic field B_1 ($B_1 << B_0$). Aplication of B_1 causes precession in it's direction. In a frame of reference relative to MRI system (fig. 2.1 (A)), superposition of B_0 caused and B_1 caused precession would be required to describe position of nuclear magnetic momet vector in time. It is then conventional to describe these manipulations in frame of reference, rotating around z axis with angular frequency equal to Larmor frequency (fig. 2.1 (B)), so that it eliminates the B_0 caused precession.

2.4. Excitation and relaxation

It was already mentioned, that with only B_0 applied, net magnetization vector only has a longitudinal component. From practical point of view, it is almost impossible to detect magnetization of the intensity provided by single voxel, in B_0 direction, because B_0 intensity is greater about several orders. The solution to this problem is to tilt the net magnetization into transverse plane, where it is far easier to measure.

2.4.1. Excitation

The tilting can be achieved by applying circularly polarized magnetic field B_1 in direction of x axis. In laboratory frame of reference such field is described by (2.15)

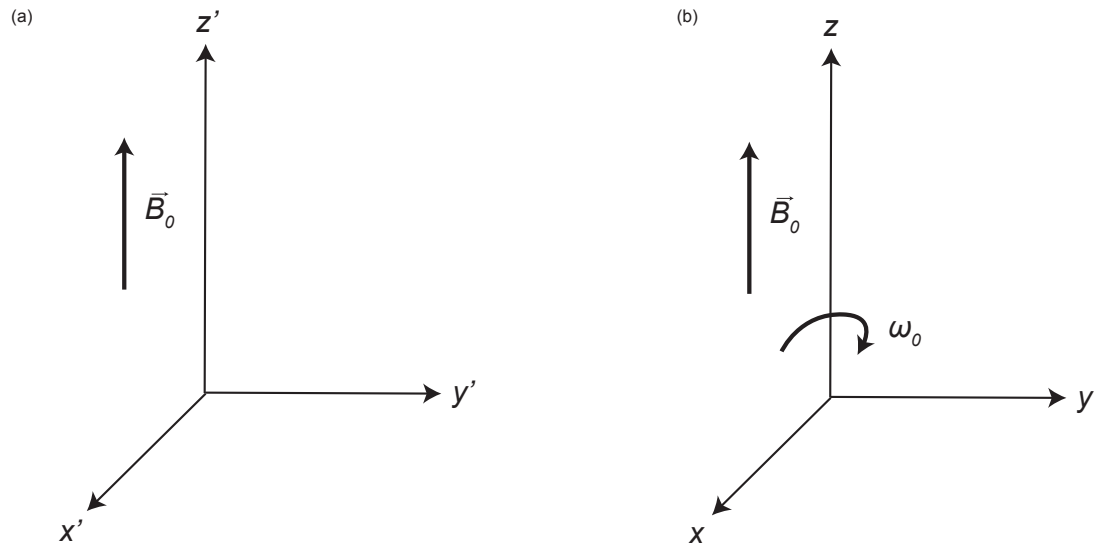

Figure 2.1: Laboratory (a) and rotating (b) frames of reference.

$$\vec{B_1^{cir}} = B_1(\hat{x}cos(\omega t) - \hat{y}sin(\omega t)) \tag{2.15}$$

To allow any tilting of M_0, the angular frequency ω must be equal to Larmor frequency ω_0 given by (2.8), this request is called the on-resonance condition. Activation of the B_1 magnetic field for a period of time τ is refered to as radiofrequency pulse. Supposing that the on-resonance condition is met, the RF pulse tilts the vector of net magnetization about angle ϕ given by (2.16) with respect to z axis.

$$\phi = \gamma B_1 \tau \tag{2.16}$$

It can be observed, that $M_{\parallel}$ is decremented, whereas $M_{\perp}$ is incremented proportionally. This process is called excitation.The relaxation process starts immediately after activating B_1 field and takes place for certain time after the end of excitation. Relaxation, in fact, consists of 2 different mechanisms, which will be presented separately.

2.4.2. Spin-Lattice relaxation

Let us consider the vector of net magnetization M_0 to be tilted about arbitrary angle, then the value of M_Z is smaller than initially. Due to the interaction between individual spins and surrounding lattice, the longitudinal magnetization grows into its original state. The rate of change is proportional to the difference between magnitude of M_0 and value of longitudinal magnetization, which represent additional term for (2.13). Thus the rate is given by (2.26).

$$\frac{d\vec{M}_z}{dt} = \frac{1}{T_1}(M_0 - M_z) \tag{2.17}$$

The constant of regrowth in (2.26) is called spin-latice or T_1 relaxation time. The value of T_1 represents time needed by longitudinal magnetization to regain 63% of it's

initial value after 90° RF pulse. It is differs for diferent kinds of tissues, molecules, etc., thus the T_1 value must be measured for each of them. Solution of (2.26) yields equation determining value of longitudinal magnetization in time.

$$M_z(t) = M_z(0)e^{\frac{-t}{T_1}} + M_0(1 - e^{\frac{-t}{T_1}}) \tag{2.18}$$

In (2.29), time 0 relates to the beginning of excitation and M_0 stands for magnitude of net magnetization vector.

2.4.3. Spin-Spin relaxation

After excitation all nuclear spins are in phase, and thus, since they no longer cancel out each others magnetization, form a nonzero transversal magnetization. However the local field inhomogeneities introduced by fields generated by neighbouring spins and local B_0 inhomogenities lead to local variations of Larmor frequencies and by extension to dephasing and lose of transversal magnetization's magnitude. Consequently a decay term is to be added to (2.19).

$$\frac{d\vec{M}_\perp}{dt} = \gamma\vec{M}_\perp \times \vec{B} - \frac{1}{T_2^*}\vec{M}_\perp \tag{2.19}$$

In rotating frame of reference (2.19) can be simplified into (2.20).

$$\frac{d\vec{M}_\perp}{dt} = -\frac{1}{T_2^*}\vec{M}_\perp \tag{2.20}$$

The constant of decay in (2.20) is is composed (2.21) of constants representing the influence of neighbouring spins (T_2) and the influence of local B_0 inhomogeneities ($T_{2'}$)

$$T_2^* = \frac{T_2 T_{2'}}{T_2 + T_{2'}} \tag{2.21}$$

The T_2 is called spin-spin or T_2 relaxation time. The value of T_2 represents time needed by transversal magnetization's magnitude to decay to 37% of it's value after 90° RF pulse. Some approximate values of T_1 and T_2 for various organic tissues are listed in Table (2.1). Solution of (2.20) yields equation determining value of transversal magnetization in time.

$$\vec{M}_\perp(t) = \vec{M}_\perp(0)e^{\frac{-t}{T_2^*}} \tag{2.22}$$

Figure 2.2 shows the regrowth of longitudinal and the decay of transversal magnetization's magnitude for relaxation times of the tissues listed in Table 2.1.

Table 2.1: Table of approximate T_1 and T_2 values of some basic kinds of tissues

Sample	$T_1[ms]$	$T_2[ms]$
Blood	1200	250
Muscle	900	50
Fat	250	60
Cerebrospiral fluid	4500	2200
White matter	600	80

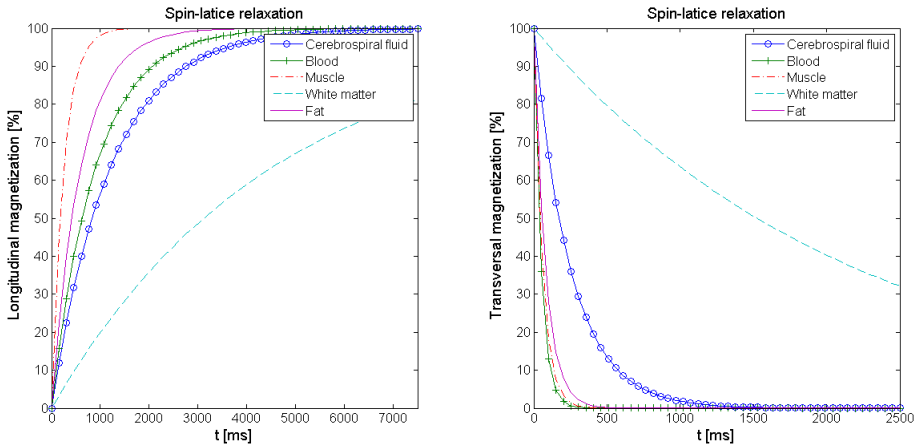

Figure 2.2: Progression of longitudinal and transversal magnetization after 90° RF pulse.

2.4.4. Bloch equations

The longitudinal magnetization relaxation equation (2.26) and the transversal magnetization relaxation equation (2.20) can be combined into eq. (2.23) describing change of net magnetization in time in rotating frame of reference. Equation (2.23) is refered to as the Bloch equation.

$$\frac{\vec{M}(t)}{dt} = \frac{1}{T_1}(M_0 - M_Z)\hat{z} - \frac{1}{T_2}\vec{M}_\perp \tag{2.23}$$

The forms of (2.23) for change of magnetization in individual directions are given by equations (2.24),(2.25),(2.26), often refered to as Bloch equations.

$$\frac{\vec{M}_x(t)}{dt} = \omega_0 M_y - \frac{M_x}{T_2} \tag{2.24}$$

$$\frac{\vec{M}_y(t)}{dt} = -\omega_0 M_x - \frac{M_y}{T_2} \tag{2.25}$$

$$\frac{\vec{M}_z(t)}{dt} = \frac{(M_0 - M_z)}{T_1} \tag{2.26}$$

SSubsequent analytic solutions of (2.24),(2.25),(2.26) provided in [6] are given by (2.27), (2.28), (2.29).

$$\vec{M}_x = e^{-\frac{t}{T_2}}(M_x(0)cos\omega_0 t + (M_y(0)sin\omega_0 t) \tag{2.27}$$

$$\vec{M}_y = e^{-\frac{t}{T_2}}(M_y(0)cos\omega_0 t - (M_x(0)sin\omega_0 t) \tag{2.28}$$

$$\vec{M}_z = M_z(0)e^{-\frac{t}{T_1}} + M_0(1 - e^{-\frac{t}{T_1}}) \tag{2.29}$$

If a coil is placed close enough to a sample in magnetic field B_0 and the sample is excited by 90° RF pulse, it is able to observe changes of magnetization described by Bloch equations. It's due to well known Faraday's law of electromagnetic induction.

After connecting the coil to AD convertor and displaying signal, one would see oscillating, decaying signal. The signal is given by a summ of the magnetization of spins in excited area, which is referred to as free induction decay.

2.5. Gradients

The use of gradient coils, also known as gradients, was introduced independently by Lauterbur and Mansfield in 1974. Gradient coils are capable of producing linearly, spatially varying magnetic field (gradients) if switched on, so that the intensity goes from negative to positive values, and there is zero magnetic field intensity in its center. They are perpendicular on each other as shown in Figure 2.3. , so they can produce field increase in x, y, and z direction. Spatial and temporal variation of magnetic field intensity is crucial to spatially encode a NMR signal, so later an MRI image can be formed [5].

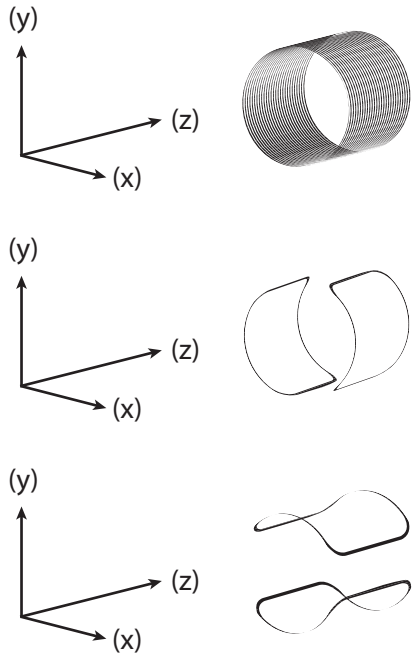

Figure 2.3: Gradient coils shape

Increments of magnetic field intensities are added to the main magnetic field intensities, so basically any bulk of sample can experience slightly different magnetic field. We call these bulks isochromates, and define them as packs of protons precessing with the same frequency. The gradient vector $\vec{G}$ is described by (2.30).

$$\vec{G} = \frac{\partial B_z}{\partial x}\hat{x} + \frac{\partial B_z}{\partial y}\hat{y} + \frac{\partial B_z}{\partial z}\hat{z} \equiv G_x\hat{x} + G_y\hat{y} + G_z\hat{z} \tag{2.30}$$

Here e.g. G_x denotes gradient in the x direction, i.e. the change of B_z component along the x axes. [5]. And the isochromates, experience magnetic field $\vec{B}$ given by (2.31)

$$\vec{B} = (B_0 + G_x x + G_y y + G_z z)\hat{z} \tag{2.31}$$

From the construction point of view it is desirable to minimize inductance and resistance of the coil. The lower the inductance is, the less energy accumulates in the coil after it's switched on, and thus it can be switched on and off faster. The value of resistance affects the energy dissipation. The performance of gradient coils is given by following properties. Gradient strength $[T \cdot m^{-1}]$ yields the maximal achievable spatial variation of gradient field. Slew rate $[T \cdot m^{-1} \cdot s^{-1}]$ describes rate of change of gradient field. Although MRI is generally accepted as a harmless imaging modality, the slew rate is being limited to avoid peripheral nerve simulation and other biological effects.

3. Image reconstruction from non-Cartesian data

Standard way to reconstruct an image from a Cartesian set of k-space data is the use of the inverse fast Fourier transform. The problem is that the IFFT cannot be used for data laying on a non-Cartesian raster. For non-uniformly sampled data the IDFT can be employed, but it is vastly computationally demanding [5]. With the expanding use of non-Cartesian data acquisition, various algorithms were introduced. In this thesis, algorithms promising sufficient results with reasonable computational load will be discussed and tested. The most suitable algorithm is to be implemented to MRI system of ISI of the ASCR, v. v. i. in later progress.

3.1. Discrete Fourier transform

It was already mentioned, that DFT is not suitable for direct image reconstruction from non-Cartesian data. However, some later discussed methods include the 2D IDFT so it's worth introducing its concept. The DFT (3.1) yields a finite spectral content of discrete signal and vice versa, the inverse discrete Fourier transform IDFT (3.2) yields approximation of discrete signal from its spectrum. In other words it transforms the signal from the frequency to the spatial (image) domain and vice versa.

$$F(k_x) = \frac{1}{\sqrt{N}} \sum_{x=0}^{N-1} f(x) \cdot e^{\frac{-j2\pi k_x x}{N}} \tag{3.1}$$

$$f(x) = \frac{1}{\sqrt{N}} \sum_{k_x=0}^{N-1} F(k_x) \cdot e^{\frac{j2\pi k_x x}{N}} \tag{3.2}$$

Extension into second dimension yelds 2D DFT (3.3) and 2D IDFT (3.4).

$$F(k_x, k_y) = \frac{1}{N} \sum_{x=0}^{N-1} \sum_{y=0}^{N-1} f(x, y) \cdot e^{\frac{-j2\pi(k_x x + k_y y)}{N}} \tag{3.3}$$

$$f(x, y) = \frac{1}{N} \sum_{k_x=0}^{N-1} \sum_{k_y=0}^{N-1} F(k_x, k_y) \cdot e^{\frac{j2\pi(k_x x + k_y y)}{N}} \tag{3.4}$$

- N ... number of samples
- k_x, k_y ... position of a data point in spatial frequency domain
- x, y ... position of a data point in spatial domain
- $F(k_x, k_y)$ ... the complex value of a data point at a given position in frequency domain
- $f(x, y)$ ... the complex value of a data point at a given position in spatial domain

3.2. Gridding

Gridding algorithm was originally introduced by O'Sullivan in 1985 [10]. Since then it underwent a lot of innovations, but the idea remains the same. The purpose of the gridding generaly is to resample non-uniformly sampled data to uniform pattern (see figure 3.1) so they are suitable for applying 2D IFFT.

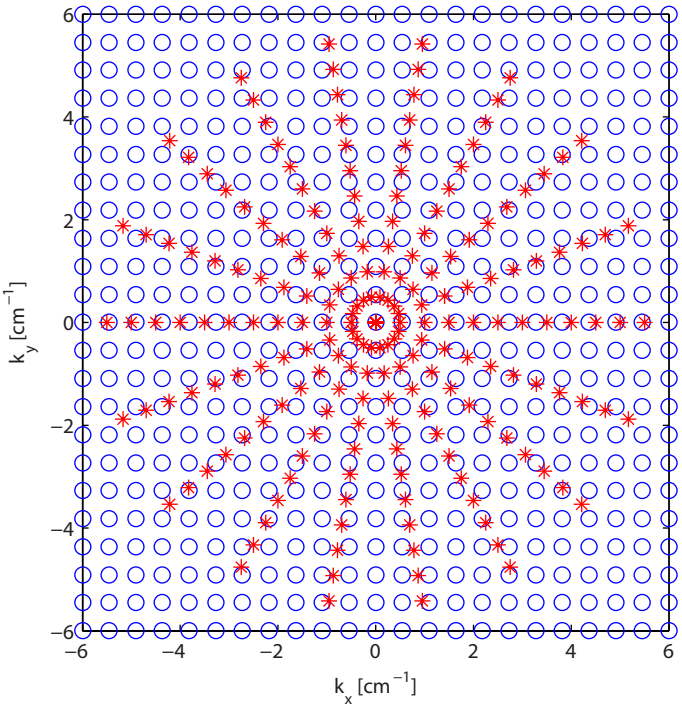

Figure 3.1: Non-Cartesian k-space data (stars) and Cartesian grid (circles) to which they need to be sampled prior to the IFFT.

Since the table-enhanced gridding [12] will be introduced later on, the formalism used therein will be respected in this section for the sake of simplicity. The value of a single grid point is determined by (3.5).

$$F(k_x, k_y) = \Big[C(k_x, k_y) * \sum_{i=0}^{N_S-1} (\rho^{-1}(k_x(i), k_y(i)) \cdot G(k_x(i), k_y(i)) \cdot \delta(k_x - k_x(i), k_y - k_y(i)))\Big] \cdot comb(k_x, k_y) \quad (3.5)$$

The equation 3.5 combines the first 3 steps in the gridding algorithm:

1. The non-uniform sampling comes with variations of local sampling densities $\rho(k_x, k_y)$. Thus it's common to compensate the density of the k-space data $G(k_x(i), k_y(i)) \cdot \delta(k_x - k_x(i), k_y - k_y(i))$ by multiplying it by the density compensation function (DCF) $\rho^{-1}(k_x, k_y)$. There are several ways to determine appropriate DCF, let us take a look at two of them.
   Analytical derivation. When the k-space positions are given by function prescription, it is posible to analyticaly derive the coefficients of DCF. $\rho^{-1}(k_x, k_y)$
   Voronoi diagram. In Voronoi diagram (see figure 3.2) the space of the cell around each data point is proportional to the sampling density, so it can be used to determine the coefficients of DCF.

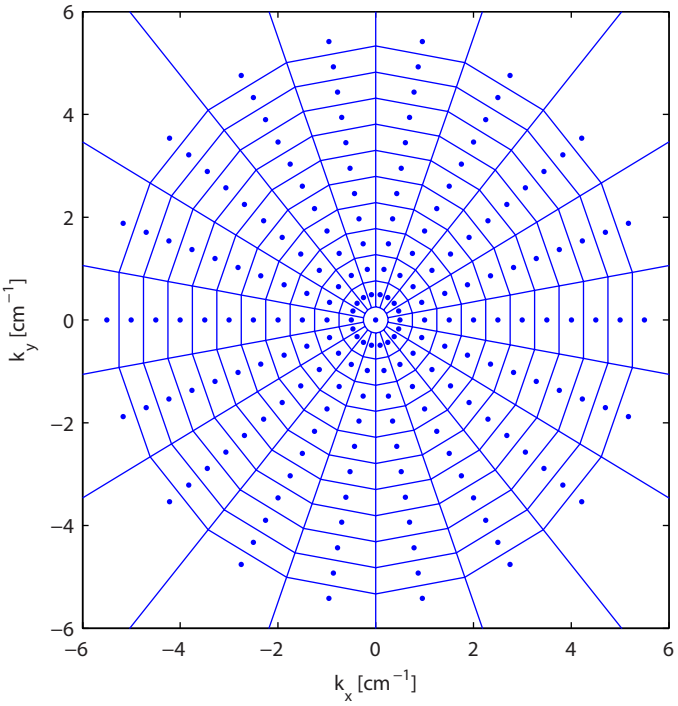

Figure 3.2: Voronoi diagram of k-space data shown in figure 3.1

.

2. Convolving the data with a convolution kernel $C(k_x, k_y)$ Jackson *et al.* suggest the use of the Kaiser-Bessel function in [13].

3. To actually resample the data on to a cartesian grid, the convolved data are multiplied with a *comb* function (3.6).

$$comb(k_x, k_y) = \sum_{u=0}^{N-1} \sum_{v=0}^{N-1} \delta(k_x - u, k_y - v) \tag{3.6}$$

4. 2D IFFT is applied to $F(k_x, k_y)$ data. To transform the data from k-space into the spatial domain.

5. Roll-of correction, i.e. eliminating image artefacts resulting from convolution with kernel of finite extent, is performed by dividing the image data by the IDFT of the convolution kernel.

3.3. Lookup table

Dale *et al.* presented the use of the well-known concept of lookup tables for accelerating image reconstruction from non-Cartesian data in [12]. It is based on prior knowledge about the k-space trajectory, which permits performing some part of the computation in advance and thus shortening of the reconstruction. In [12], an application of LUT for accelerating the DFT and gridding is presented.

3.3.1. Table-enhanced DFT

The principle of this method will be described on a 1D signal case. For the expansion to 2D and the detailed algorithmic description see [12]. The DFT of a non-uniformly sampled signal component $F(k(i))$ i.e. its contribution to data point $f(n)$ in a spatial domain, can be determined by solving (3.7).

$$f(n) = \frac{1}{\sqrt{N}} \sum_{i=0}^{N_S-1} \rho^{-1}(k(i)) \cdot F(k(i)) \cdot e^{\frac{j2\pi k(i)n}{N}} \quad n = 0, 1, \ldots, N-1 \tag{3.7}$$

Here N_S and N denote number of samples of measured data (frequency domain) and number of samples of resulting data (spatial domain). The reciprocal value of the local sampling density $\rho^{-1}(k(i))$ stands for a coeficient of the density compensation function (see chapter 3.2 for more details). Supposing, that the k-trajectory $(k(i))$ is known, it is possible to substitute (3.7) for (3.8).

$$f(n) = \sum_{i=0}^{N_S-1} T(i, n) \cdot F(k(i)) \quad n = 0, 1, \ldots, N-1 \tag{3.8}$$

The $T(i, n)$ values can be precomputed using (3.9) and stored. They can be recalled after acquiring or when processing data point $F(k(i))$ and used in (3.8). This results in performing the DFT using only addition and multiplication.

$$T(i, n) = \frac{1}{\sqrt{N}} \rho^{-1}(k(i)) \cdot e^{\frac{j2\pi k(i)n}{N}} \quad n = 0, 1, \ldots, N-1 \quad i = 0, 1, \ldots, N_S-1 \tag{3.9}$$

This approach is stated to dramatically reduce the computional burden of DFT for non-Cartesian data, so that it becomes comparable to other reconstruction techniques.

3.3.2. Table-enhanced gridding

The table-enhanced gridding, as well as the table-enhanced DFT, is based on prior knowledge about the k-space trajectory. Consider equation 3.5. In case of known $k_x(i), k_y(i)$, (3.5) can be substitued with (3.10)

$$F(k_x, k_y) = \sum_{i=0}^{N_S-1} T(i, k_x, k_y) \cdot G(k_x(i), k_y(i)) \tag{3.10}$$

The $T(i, k_x, k_y)$ values can be pre-computed, stored and reloaded during the actual gridding, which, in conclusion, consists of multiplication and addition.

$$T(i, k_x, k_y) = C(k_x, k_y) * (\rho^{-1}(k_x(i), k_y(i)) \cdot \delta(k_x - k_x(i), k_y - k_y(i))) \cdot comb(k_x, k_y) \quad i = 0, 1, \ldots, N_S-1 \tag{3.11}$$

3.4. Non-uniform Fast Fourier transform

The general concept of fast Fourier transform of non-uniformly sampled data was brought by Dutt and Rokhlin in [14]. Since then it became the point of interest of many researchers. The use of non-uniform Fast Fourier transform (NUFFT) for processing of non-Cartesian MRI data was proposed by Yang and Mathews in [15]. In their later work Yang and Mathews optimized NUFFT and presented the method of Mean square optimal NUFFT approximation [9].

The NUFFT is used by iterative reconstruction algorithms. The non-uniform Fourier samples are evaluated as the over-sampled uniform FFT of the image model, weighted by appropriate scale factors. The selection of the ideal scale factors and interpolators is described in detail in [15] and [9]. It is stated that by choosing the ideal combination of scale factors, interpolators and error metric, the need of above mentioned over-sampling is reduced. Mathematical description of the NUFFT is rather too complicated to be meaningfully described here.

4. K-trajectory measurement methods

Exploitation of fast imaging techniques comes with a significant demand on k-space trajectory fidelity, especially with non-Cartesian sampling. The k-space trajectory is depends on a gradient system in particular, hence determining actual gradient waveforms and comparing them to theoretical waveforms can yield some information about the k-trajectory fidelity.

4.1. Gradient impulse response function

Quite an elegant method for measuring the gradient waveforms is presented by Liu and Matson in [7]. This method is based on the input-output characteristic of system (4.1), in this case gradient system. Once you get the information about this system via measuring $h(n)$. You can apply this information on arbitrary theoretical gradient waveform to estimate the actual gradient waveform.

$$out(n) = \sum_{i=-\infty}^{\infty} in(i) \cdot h(n-i) \tag{4.1}$$

Here in denotes the input signal, i.e. theoretical gradient waveform, and out stands for output of system, i.e. actual gradient waveform. The function h carries information about system. By applying convolution theorem, (4.1) can be substituted with (4.2).

$$OUT(m) = IN(m) \cdot H(m) \tag{4.2}$$

Where $IN(m)$, $OUT(m)$, $H(m)$ are Fourier transforms of $in(n)$, $out(n)$ and $h(n)$. $H(m)$ is then called the gradient impulse response function (GIRF).

This method considers the gradient system to be linear, time invariant system. Such condition is met within normal scanning conditions regarding limited gradient strengths and FOV, and recommended slew rates and duty cycles. After certain simplification this algorithm can by described as follows:

1. System output for known input is measured.
2. Computation of GIRF coeficients.
3. Applying of GIRF to arbitrary theoretical waveform.

As stated, GIRF approach is elegant, it however requires special hardware, and thus it is out of the scope of this thesis. Notable advantage is that after step 2 of the algorithm above, the actual gradient waveform can be estimated without access to MRI system.

4.2. Phase variation method

The simple phase method introduced by Latta *et. al.* [8] computes the actual gradient waveform out of the information about phase variation introduced into the signal by the given gradient. It doesn't require any special hardware, just a spherical phantom filled with doped watter.

The algorithm consists of 2 measurements. First one proceeds as shown in figure 4.1. It starts with selective excitation of a slice perpendicular to examined gradient axis and located out of gradient isocenter. The excitation is followed by a rephasing lobe of the slice selection gradient. Next the gradient pulse is applied, simultaneously with the start of acquisition. The second measurement serves as a reference, its purpose is to eliminate eddy current artefacts from gradient switching. This measurement differs from the first one only by not activating the measured gradient.

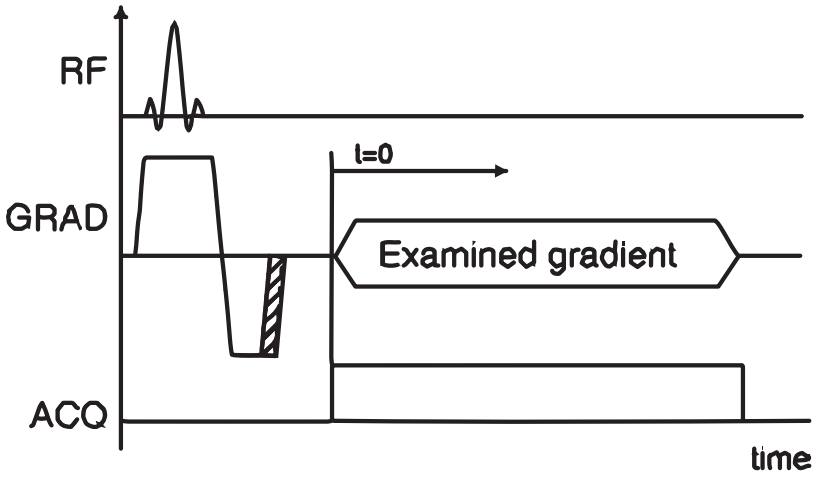

Figure 4.1: Pulse sequence for phase variation method [8]

The phase diference between the phases of signals of both scans ($s_{grad}(t)$,$s_{ref}(t)$) in the time t is given by (4.3). In this example, we use the x gradient.

$$\Delta\Phi_x(t) = phase(s_{grad}(t)) - phase(s_{ref}(t)) \tag{4.3}$$

The gradient waveform $G_x^{'}$ is then calculated from (4.4).

$$G_x^{'} = \frac{\Delta\Phi_x((n+1)\Delta t) + \sigma_{n+1}(\phi) - \Delta\Phi_x(n\Delta t) - \sigma_n(\phi)}{\gamma D_x \Delta t} \tag{4.4}$$

Here $\Phi_x(n\Delta t)$ denotes the phase difference between the n-th samples of signals measured with and without activated examined gradient, Δt is the sampling period (dwell time), $\sigma_n(\phi)$ denotes the standard deviation of the phase, and D_x is the distance of the slice from gradient isocentre.

This experiment provides several information about gradient pulse. It can also be used to measure short-term eddy curent anomalies during gradient switching.

5. Ultra-short echo time MRI

Generally a symptom of disease can be the change of quality of a tissue, which leads to the variation of many tissue properties. One of such properties is the T_2 relaxation time. The ability of detecting and quantifying such changes can lead to the ability to diagnose related pathology. Derived methods using MRI are widely used in both research and clinical praxis. However there is a problem with molecules possessing short T_2 ($T_2 < 1\ ms$), which yield quite low signal when imaged with standard pulse sequencies *e.g.* GE. Conventionally, speaking in terms of UTE, tissues are divided [16] into those with majority of short T_2 components and those with minority of short T_2 components.

Table 5.1: Tissues with majority of short T_2 components [17].

Meninges (dura)	Falx	Tentorium
Membranes	Capsules	Bands
Retinaculi	Septae	Fascae
Sheaths	Nails	Hair
Aponeuroses	Tendons	Ligaments
Menisci	Labrii	Periosteum
Bone	Dentine	Enamel

MRI of tissues with majority of short T_2 components was known to be theoretically possible, but it was limited by technology progres for some time. However modern MRI systems are capable of performing UTE pulse sequence, sequence with significant demand on RF and gradient systems.

5.1. Pulse sequence and system demandss

The pulse sequence for UTE MRI is somewhat similar to the GE pulse sequence, although it doesn't even form echo in most cases. It uses several mechanisms to accelerate the acquisition process, so it can get down to TE of approximately $10\mu s$. Mechanisms such as half excitation pulse, radial k-space sampling, acquisition on gradient ramp and the absence of slice refocusing pulse. You can see theoretical UTE pulse sequence in fig. 5.1.

With conventional pulse sequences excitation time doesn't have to be taken into account, because only negligible relaxation of long T_2 components takes place in respective time period, but it is to be considered in case of UTE. Therefore half-Gauss (truncated) RF pulse is being exploited, allowing excitation times in order of tenths of millisecond. In order to transmit energy equal to long excitation pulses, the pulses used in UTE must be of great peak value. There are two issues related to the peak value of B_1, first one is purely technical, the RF system must be capable of producing it. Then there is the safety issue, since there is a limit for peak value of B_1 for use on humans. Moreover the truncation of the pulse trades of the quality of excitation which has to be either corrected or taken into account.

In comparison with rectangular k-space sampling, the trajectory of radial sampling is shorter, as it doesn't have to travel to the edge of k-space prior to acquisition. Radial sampling starts in the middle of k-space where no gradients are needed. Moreover, there is no need for phase encoding gradient, neither for read dephase gradient. To minimize the

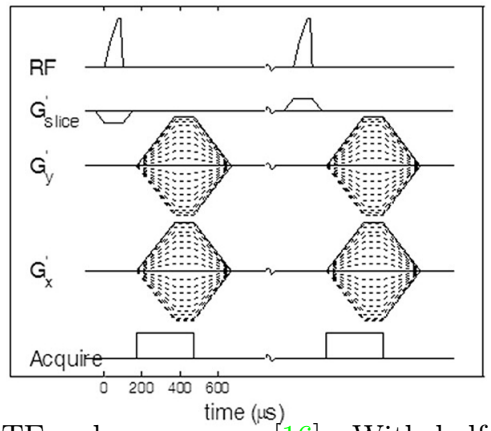

Figure 5.1: Theoretical UTE pulse sequence [16]. With half-pulse excitation, on-ramp acquisition and radial k-space sampling. Without slice rephasing gradient.

TE, the data acquisition starts on the gradient ramp, which results in non-equidistant sampling of some of the initial points. Non-equidistant spacing must be included in trajectory calculation.

It is conventional in UTE to omit slice rephasing lobe and perform scan twice, once with positive slice selection gradient and seconds with negative slice selection gradient, colected data are then added. This way, no actual echo is formed. Handicap of this mechanism lays in doubling the total acquisition time, which is now given by (5.1), where n is number of points per projection.

$$T = 2\pi n T_R \tag{5.1}$$

Pulse seqence described above impemented on suitable MR system allows to achive ultra short TE. So that signal from tissues with short T_2 is obtained, and imaging of tissues with majority of short T_2 components. But for imaging tissues with majority of long T_2 components, the signal from long T_2 components is to be suppressed in some way. The most common approach to get rid of this signal is to rotate long T_2 components with a long (*eg* $10ms$) rectangular pulses to transverse plane, dephase them with a crusher gradient, and then perform UTE sequence. Larson *et al* [18] propuse method adiabatic inversion pulses. Another method uses image subtraction of images measured with TE in the interval from TE_{min} to TE which leaves the long T_2 components' signal only.

5.2. Applications

Bergin et al [21] were the first to implement UTE sequences on MR system in Stanford to use it for lung imaging. Since then it spread its use to various tissues. Anyway, there still are limitations in human use, due to the need for significant gradient slew rate and B_1 intensity. Robson *et al* describes imaging of bones and conective tissue in [19]. There are many studies using UTE MRI for studying various properties of brain, for example myelinization [20]. Or the lung tissue imaging [21].

6. Echo planar and Spiral MRI

Echo planar imaging and Spiral are methods enabling ultra fast MR image acquisition developed by Mansfield [22] in 1977 and Mayer in 1998. State of the art MRI systems are capable of acquire image in tens of milliseconds. The EPI and derived sequences, such as spiral, ment a true breakthrough in MRI. Because it brought rather revolutionary, today considered routine, applications such as i fMRI, DTI or real-time MRI.

6.1. EPI

The pulse sequence of EPI (figure 6.1) is specific by after one RF excitation,instead of one echo, a series of echoes denoted as echo train is formed. To do so, EPI exploits series of readout gradient pulses of both polarities. Besides readout gradients, the phase encoding gradient is being used to add horizontal spatial encoding. It's to be mentioned, that EPI images generally possess a low resolution due to the fact, that number of echoes is limited by relaxation. Higher resolution can be achieved by multiple excitations, each of which acquires an area of k-space, which, of course, is a tradeoff for acquisition time.

Figure 6.1 displays 2 common EPI pulse sequences. Both of them start with prephasing gradient, folowed by the series of bipolar readout gradient oscilations. The difference comes with the phase encoding gradient, in case of the (a) sequence, the phase encoding gradient is of constant value for the duration of acquisition, forming zig-zad trajectory. In the (b) sequence, the phase encoding gradient is switched for a short period of time to be able to encode next line of k-space, such way of treating the phase encoding gradient is refered to as bliped EPI. The trajectories of such sequences are not necessarily linear, moreover sampling periods are not uniform, due to on-ramp sampling. These information are to be considered in recionstruction.

6.2. Spiral

Spiral and EPI pulse sequences are being similar to some extent, both of them are able to form image after one excitation. The spiral trajectory is advantageous from certain perspective. It starts in the centre of the k-space which enables quick start of acquisition and thus short TE, so that it is suitable for UTE imaging. Field of view of spiral trajectory is circular and omits corners, which might be considered effective with presumption, that that most of the energy of MRI signal is located in central area. Gradient waveforms forming spiral trajectory are more effective, than with some of EPI sequences, because they are being changed continuously. Same as EPI, the spiral acquisition can be both single-shot and multishot, with advantages and trade offs similar to EPI.

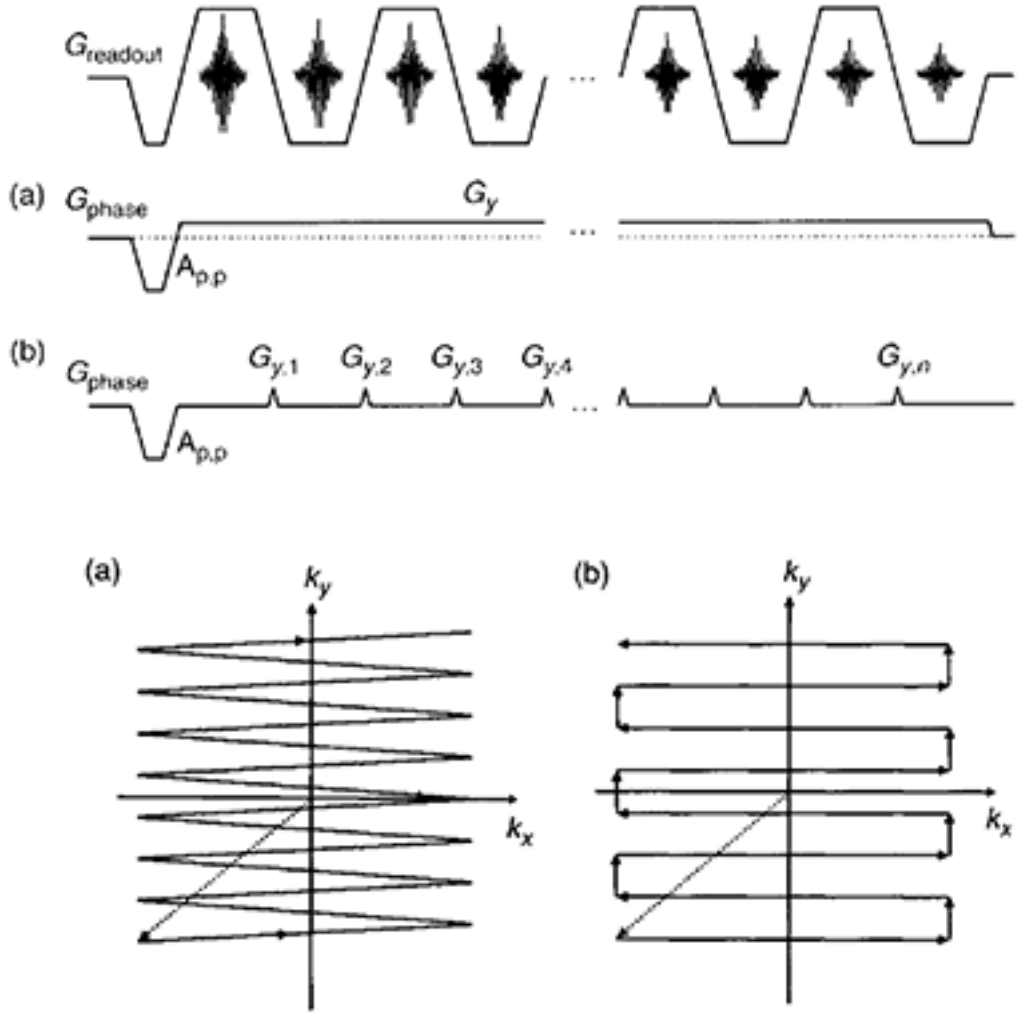

Figure 6.1: Two typical pulse sequences for EPI (a) the zig zag EPI, (b) the bliped EPI.

7. Image reconstruction

7.1. Software solution

Gridding was chosen to be the reconstruction method, since it is relatively easy to understand and thus to debug when implemented. The main output of this thesis was then agreed to be gridding function with defined interface, therefore the data-preprocessing layer has to be added, to form input data into defined structure. The data pre-processing layer deals with 3 formats of data. The SW phantoms in form of .mat files, 4.7 T MRI system (detailed description of MRI systems in the ISI is given bellow) data in .mrd file, and 9.4 T MRI system data in a directory of each particular scan. In fig. 7.1 a simplified dataflow scheme summarizes the software solution programmed for this thesis.

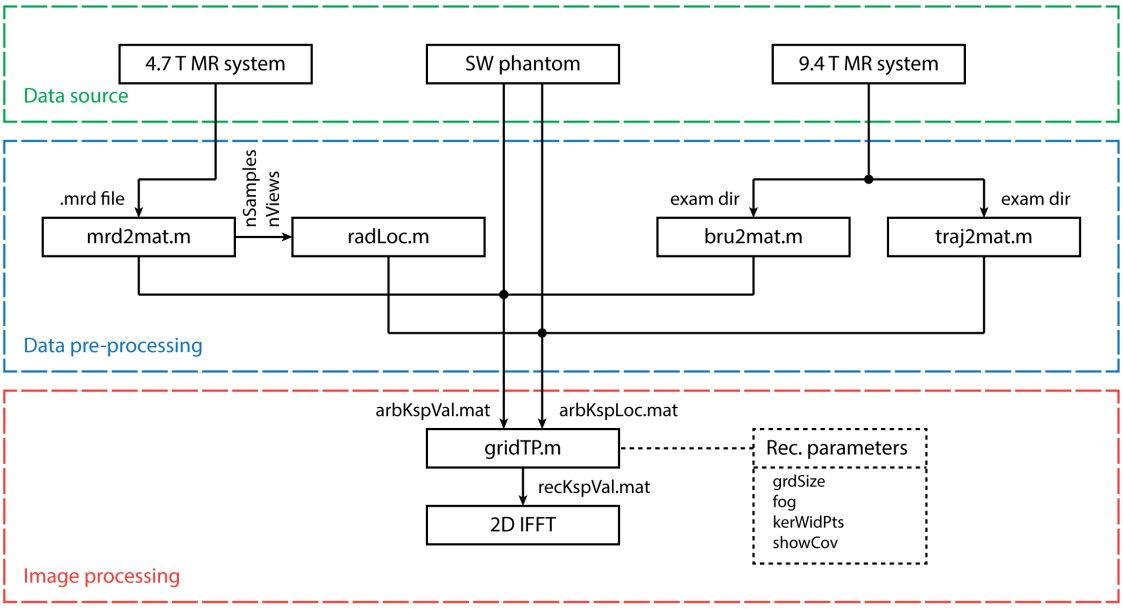

Figure 7.1: Scheme of implemented software solution.

MATLAB® was chosen to be default programming language and environment due to many reasons *e.g.* Bruker Ldt. provides MATLAB® toolbox PVTOOLS, including various data converting and displaying functions, at least then programming of one converter is spared. List of the most used variables used across all functions can be seen in table 7.1. In terms of consistency, each function posses simple logical layer, checking input arguments, so that oportune errors are limited.

In following section, description of particular functions is given, with focus on the idea of their functionality. You can find more details in comments in relevant .m files. The code examples appearing in text of this thesis might not be identical to code attached .m files, but the functionality remains unchanged.

7.1.1. Data pre-processing

Software phantoms

The SW phantoms used are being most favorable in terms of pre-processing demands. They provide both values and trajectory in .mat file, which makes them easy to be loaded and passed to reconstruction function.

4.7 T system data

The MR SOLUTIONS Ldt. 4.7 T system saves data into .mrd binary files. Basically tohse files can be divided into three sections the header, the data section, and the footer.

Function `mrd2mat.m` was created to read those data, exploiting several prior knowledges. The header and data sections are coded as signed 16 bit integers. The size of header is 256 words and it contains information about sequence in a very simple form. The key prior knowledge is, that the first word of header stores number of samples and the

Table 7.1: List of variables

Variables storing trajectories and data	
`arbKspLoc`	Arbitrary k-space locations
`arbKspVal`	Arbitrary k-space values
`crtKspVal`	Cartesian k-space values
`crtKspLoc`	Cartesian k-space locations
`kernel`	Vector of convolution kernel
`raw`	Raw data read from binary files
`recImgVal`	Reconstructed image values
Parameter variables	
`fog`	Overgridding factor
`gridSize`	Size of resulting image
`kerPts`	Convolution kernel size
`kerWid`	Convolution kernel in k-space distance
`kerWidPts`	Convolution kernel in k-space units
`nSamples`	Number of samples in projection
`nViews`	Number of projections/interleaves
`showCov`	In case it's set to 1, gridTP shows k-space coverage in real time.

third word stores number of projections (views). In the data section then, the complex walues of FID are stored in pairs in two following words. So it can be stated, that data section starts in the first word after the end of header and ends $2 * nSamples * nViews$ words later. So the `arbKspVal` data can be read by following code.

```
raw = fread(fileID,'int16');
header = 256;
for i = 1:2:2*nSamples*nViews
    arbKspVal(ceil(i/2)) = complex(raw(header+i),raw(header+i+1));
    % plot (raw(header+i),raw(header+i+1),'+')
    % drawnow
end
```

In case of any doubts about the trajectory reading, or trajectory itself, two commented rows in the cycle should be uncommented to see gathering of the trajectory points one by one. However this might appear excessively time consuming. For such case, when there is demand to see the k-trajectory as whole, the `drawnow` row shall remain commented.

Secondary functionality of this function is processing of the footer, more specificaly, to the value read desired parameter of pulse sequence. The footer seems to be coded as 8 bit unsigned integers, whose reading has to be followed by conversion to chars, using default encoding. Reading of footer is done as follows.

```
footer = fread(fileID,'char');
footer = char(footer(2*(header+dataLen)+1:end))';
footer = strsplit(footer,':');
```

Because of different encoding, the file has to be read again, with `char` option this time. The position of the footer is determined by length of the header and the data part

combined, multiplied by two, because the reading now, process by 8 bit blocks instead of 16 bit block as before. The footer is then split into field of cells containing strings with individual variables.

Function `mrd2mat.m` doesn't have defined number of input arguments. The first argument is the path to the .mrd file. The following arguments are strings containing names of variables, whose value are to be returned. These names are then looked for in individual cells. If there is match, the string in the cell is sparse again and value is read to be returned.

The 4.7 MR system, does not provide locations of data points in k-space, not to mention informations about imperfections needed to be corrected. Locations of k-space data have to be calculated, using function `radLoc.m`, which accepts the information about number of samples and projections as input. It then uses basic analytical approach to calculate radial k-space data locations.

9.4 T system data

The Bruker Ltd. 9.4 T MR system is more advanced, than 4.7 system in many ways, including output data format. The difference starts in idea of measurment hierarchy as such. There are three levels in this hierarchy, the patient, the study and the scan, each of which is located in related subfolder, each of which contains several text files storing various informations about patient, study, *etc.*. The file of individual scan contains several files with various information about pulse sequence, system settings *etc.* and most importantly, in case of non-cartesian k-space coverage, even file containing information about trajectory.

Bruker Ltd. provides MATLAB® toolbox PVTOOLS which enables loading of k-space data. The function `bru2mat.m` then returns k-space data of a scan in a directory, whose path is being passed as an argument. It uses functions from PVTOOLS, so it is in a very simple form. User only has to specify, how many channels he intends to use for further processing.

```
rawObj=RawDataObject(dirpath);
raw = rawObj.data;
raw = raw{1};
ch1 = squeeze(raw(1,:,:));
ch2 = squeeze(raw(2,:,:));
ch3 = squeeze(raw(3,:,:));
ch4 = squeeze(raw(4,:,:));
```

Unfortunatelly PVTOOLS doesn't offer any tool for processing trajectory data file. Function `traj2mat.m` then performs conversion of the traj file into .mat file. Trajectory files have a simple structure since they only store the k-space trajectory data, no additional information. The data are encoded as 8 bit floats. So with certain simplification `traj2mat.m` processes as follows.

```
raw = fread(fileID,'double');
for i = 1:2:length(raw)-1
  arbKspLoc(ceil(i/2),:)=complex(raw(i),raw(i+1));
end
```

It is possible to display loaded trajectory by uncommenting following line of code.

```
% plot (real(arbKspLoc),imag(arbKspLoc),'+')
```

7.1.2. Gridding

In this section simplified model of implemented reconstruction is presented, for more information see comments in `gridTP.m` file. First of all, the cartesian grid is generatied.

```
grdPoints = round(grdSize*fog);
grdLine = linspace (-0.5,0.5,grdPoints);
[re, im] = meshgrid (grdLine);
crtKspLoc = flipud(complex (re,im));
```

Kaiser-bessel function is being used as a convolution kernel. Its β value is determined automatically based the main reconstruction setting parameters, the overgridding factor α and width of convolution kernel W, using formula (7.1), introduced by Beatty *et al* [24]. The shapes of resulting convolution kernels for several combinations of reconstruction parameters are shown in figure 7.2. Regarding fact, that evaluation of KB function would have to be done in the most time critical section, the convolution kernel is precomputed and stored in LUT.

$$\beta = \pi\sqrt{\frac{W^2}{\alpha^2}\left(\alpha - \frac{1}{2}\right)^2 - 0.8} \tag{7.1}$$

Data driven gridding bassically consists of four cycles, two to chose row and column of a data values and locations, and two to chose row and column of a grid values and locations. Then there is test of distance of those two data points. It it's less than a witdth of convolution kernel, the program enters the condition section. It could be written as follows.

```
for datCl=1:nViews
    for datRw = 1:nSamples
        kPtLoc= rawKspLoc(datRw,datCl);
        for grdRw = 1:gridPoints*fog;
            for grdCl = 1:gridPoints*fog;
                grdPtLoc = recCrtKspLoc(grdRw,grdCl);
                if abs(kPtLoc-grdPtLoc)<kerWid
                                %condition section
                end
            end
        end
    end
end
```

In the condition section the interpolation takes place. The gridpoint is interpolated from data point using convolutin kernel. Tt's value is then determined by linear interpolation between two nearest LUT points.

Initially, the density compensation function was determined analytically, but this approach is relatively vulnerable to k-trajectory imperfections, which frequently occur in real systems. More specifically this thesis deals with 3 kinds of data. The SW phantoms provide k-trajectory data which might seem to be flawless, nevertheless phantoms

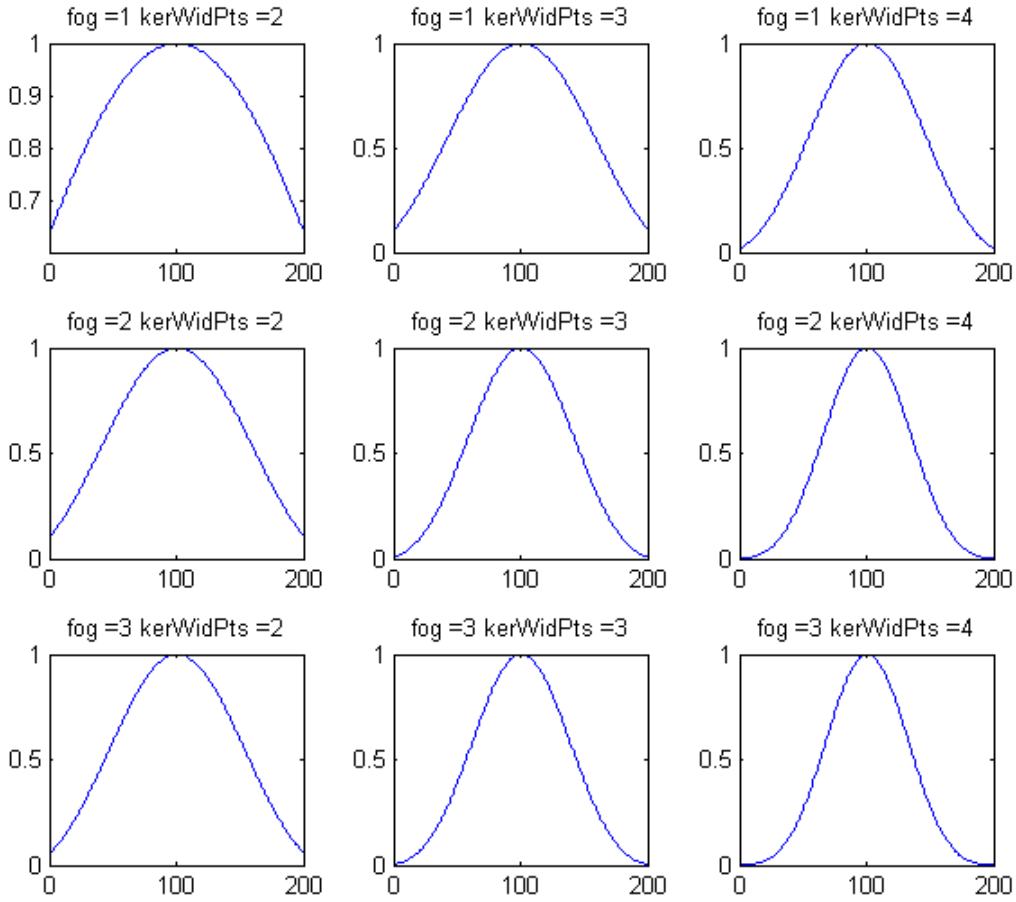

Figure 7.2: Shapes of convolution Kaiser-Bessel convolution kernels for several reconstruction parameters combinations.

provided by supervisor of this thesis Ing. Starčuk CSc., posses simulated irregularities. Real system trajectory data have, or should have undergone series of corrections so they are not suitable as well. Another solution, was meant to be the Voronoi diagram, but, it turned out to be computationally expensive, beside that related MATLAB® functions were not of consistent behavior. So at the end quite simple, but apparently sufficient method was employed. It works on the principal of a counter, every data point has it an own counter keeping information about number of additions. At the end of gridding as such, each data point is divided by the value in his counter.

7.2. Testing on radial data

To be able to determine the quality of resulting image, the reconstruction was initially tested on SW phantom provided by supervisor of this thesis Ing. Zenon Starčuk CSc.. Phantom is generated by MATLAB® script allowing to change number of projections, samples, and some other parameters disscused bellow. In fig. 7.3, you can see the phanthom and its k-space. This phantom is being interpolated onto radial grid, which, of course, introduces an interpolation error of certain extent. The total error in reconstructed

image is then given by (7.2), with e_{inter} denoting error introduced by interpolation and e_{recon} denoting error introduced by reconstruction. This fact should be considered when determining the quality of reconstruction.

$$e = e_{inter} + e_{recon} \tag{7.2}$$

Figure 7.3: Template of phantom used for testing quality of reconstruction. Original cartesian k-space data (left), zoom 5x. 2D IFFT of the k-space data (right).

In fig. 7.4 you can see radial trajectory onto which the template is interpolated. The number of samples of each projection is chosen to be 128, number of projection, to satisfy sampling criterion is then 402.

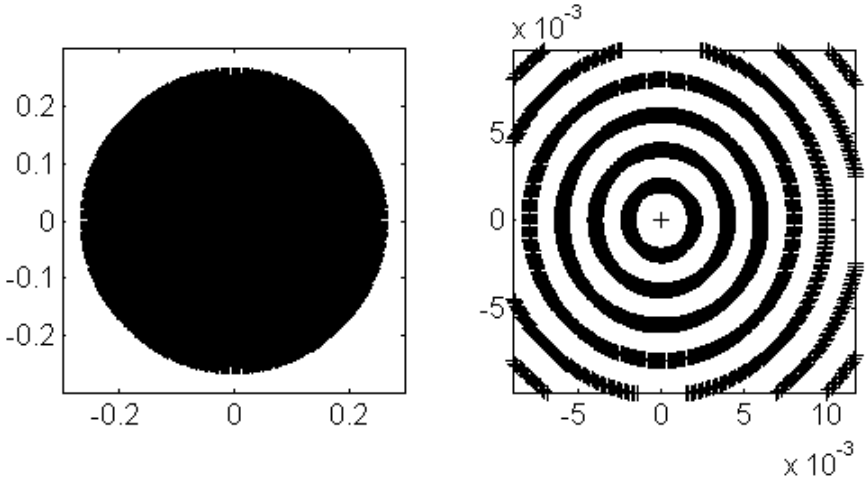

Figure 7.4: Trajectory of phantom k-space (left), zoom to the center of the k-space (right).

As stated before there are two crucial parameters of reconstruction. The overgridding factor and the width of convolution kernel in k-space units. Figure 7.5 displays the influence of overgridding factor on resulting image, wherelse figure 7.6 displays influence in k-space. Since the k-space data posses significant similarity, the images of difference between original k-space data and reconstructed k-space data is displayed, which have greater information value.

The greater the overriding factor is, the better image results. As might be noticed in figure 7.6, the influence of various values of the FOG makes distribution of energy of the difference image more homogeneous and thus the error might distribute more equally into all spatial frequencies. Whereas with low FOG *e.g.* 1, most of the energy of the difference

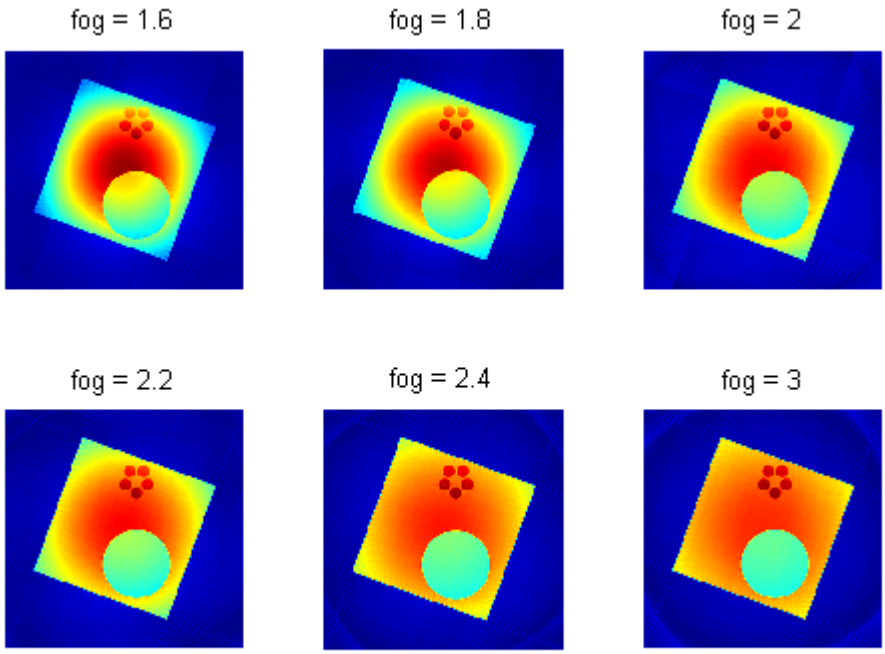

Figure 7.5: Influence of the overgridding factor on resulting image.

image is located in the centre of k-space, which results into, with certain simplification, multiplying of the image with a bell shaped function.

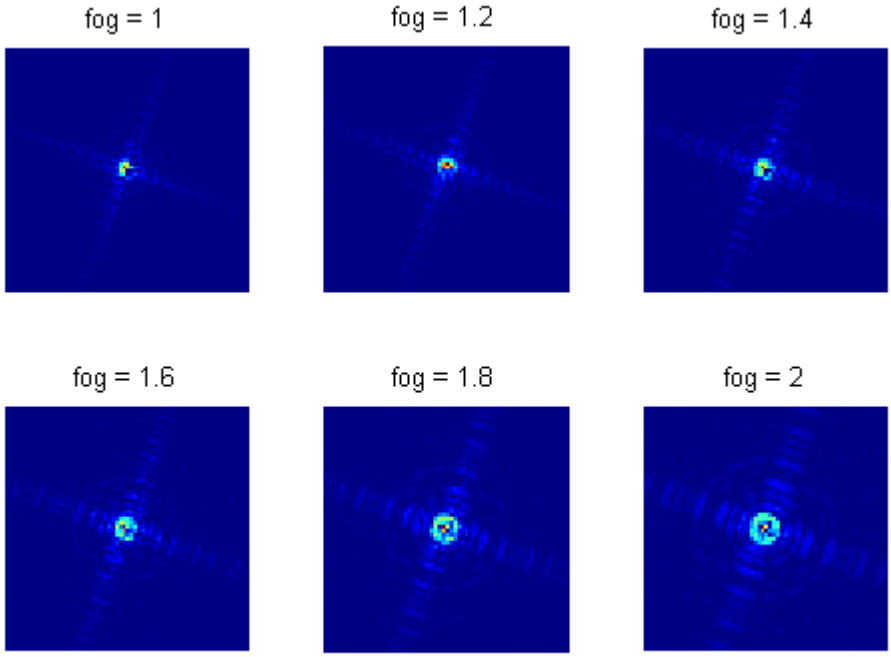

Figure 7.6: Influence of the overgridding factor on regridded k-space. To make visualization of that influence as effective as possible the difference between the original and the reconstructed k-space is shown.

Figure 7.7 displays the influence of convolution kernel width on resulting image, wherelse figure 7.8 displys influence in k-space in a same way as in prewious example.

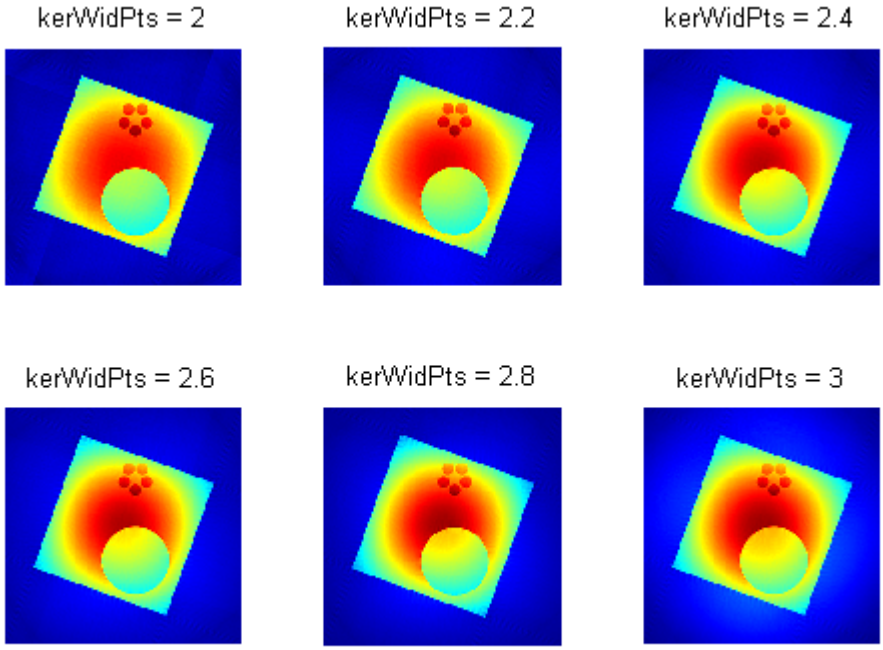

Figure 7.7: Influence of the convolution kernel's width on resulting image.

The growing width of convolution kernel seems to have actually opposite effect on the resulting image, than growing FOG. With growing kernel width, accumulation of energy can be observed in the center of the k-space of the subtraction image.

It might be deducted for this specific implementation of gridding, that ideal combination of grinding parameters would be the FOG great enough, but limited by reconstruction time, and the width of convolution kernel as small as possible, but ensuring, that even peripheral areas of the k-space will be included into convolution. Image reconstruction of with such settings can be seen in figure 7.9, which might not seem well enough, but it should be taken to account, that dynamic range of color scaled image is much greater, than at the more conveniently used gray scaled image. Grayscale representation of the very same reconstruction is shown in figure 7.10.

7.3. Polar sampling criterion violation

In this chapter, the immunity of implemented gridding reconstruction against radial sampling criterion violation. In figure 7.11 you can see 256px to 256px images, reconstructed from 402, 201 and 100 proections, *i.e.* polar undersampling 1,2,3 respectively. It could be stated, that even with polar undersampling factor of 2, relatively reasonable image can be reconstructed.

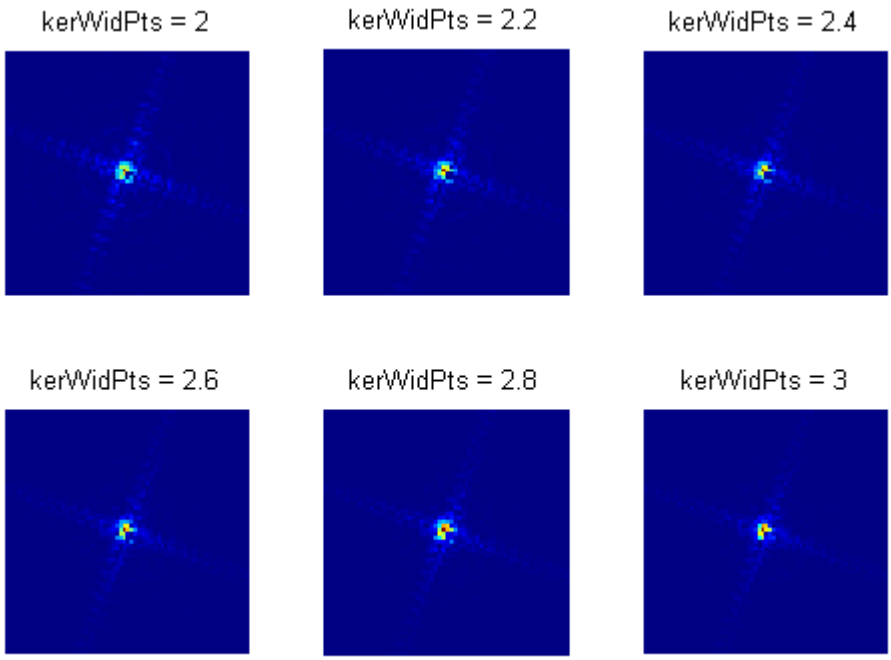

Figure 7.8: Influence of the convolution kernel's width on regridded k-space. To make visualization of that influence as effective as possible the difference between the original and the reconstructed k-space is shown.

7.4. Properties of reconstruction

In this chapter several properties of reconstruction will be disscussed. Dependence of the reconstruction parameters on the SNR and the duration of reconstruction will be examined using the data from the isolated rat brain measurement.

The influence of the reconstruction parameters was introduced in chapter 7.2. Let us see now, how varying the reconstruction parameters (the width of convolution kernel and the overgridding factor) affect the SNR of resulting image. The SNR is determined using well known formula (7.12), here the signal represents a summation of pixel values over a certain relatively homogenous part of the image with a high amplitude of signal. Noise represents a sumation of pixel values over some peripheral area.

$$SNR = 20\, log(signal/noise)\ [dB] \tag{7.3}$$

The variation is performed over a range of values where the reconstruction is meaningful *i.e.* does not introduce any significant artefact, is computionaly tolerable and interpolation takes all grid points into account. In the figure 7.12, there is an image of data, used for this analysis, with regions marked, providing the signal and noise value.

The following analysis of the duration of reconstruction is taken over the same range, so that some general advice can be given for choosing those parameters. The duration of reconstruction is measured with a dataset of 135 samples and 804 projections which is being to interpolated onto $256^2 * fog$ grid points.

Certain expectations can be confirmed and some conclusions drawn from charts in figure 7.13. First of all the reconstruction time grows far more rapidly with incrementing

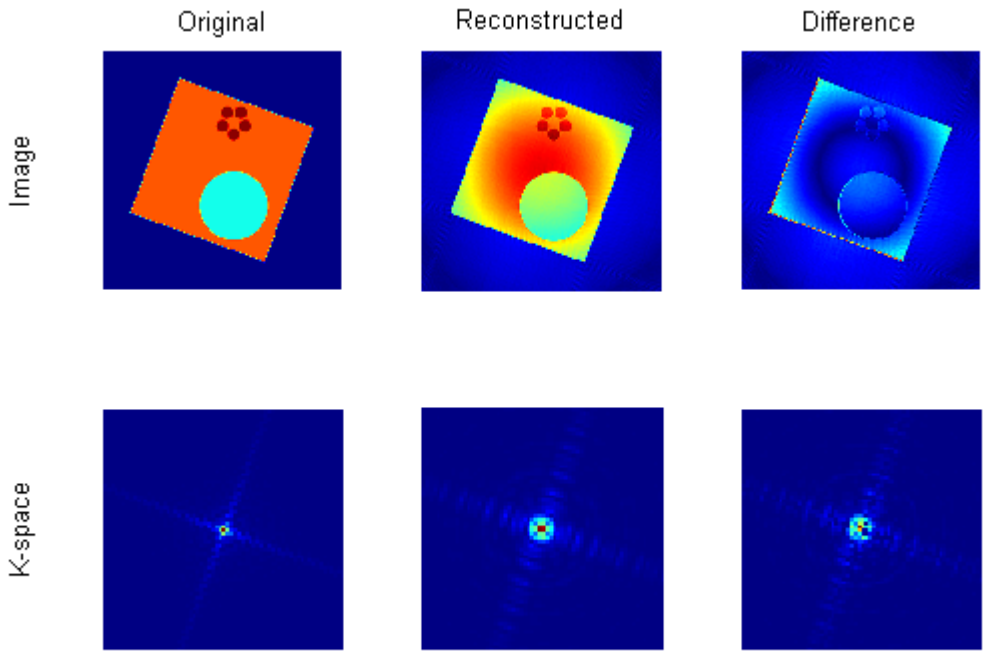

Figure 7.9: Gridding reconstruction performed with parameters seeming flavourable for reconstruction. Overgridding fatctor 2.5, and width of convolution kernel in k-space units 2.5.

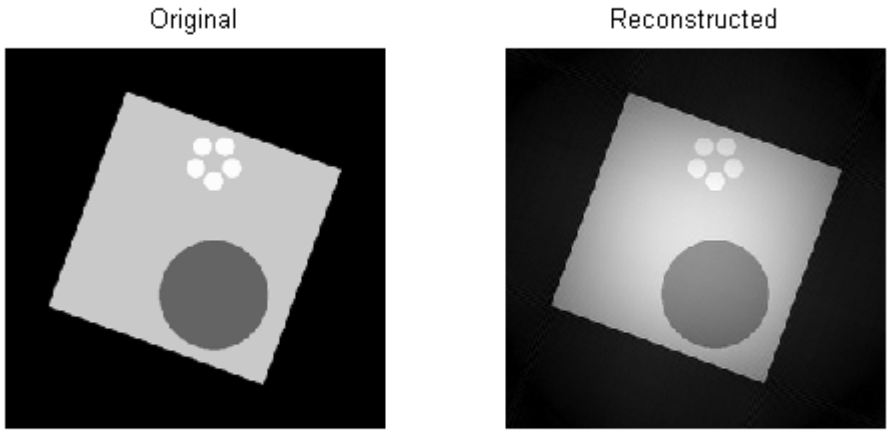

Figure 7.10: Grayscale representation of figure 7.9.

the overgidding factor, than with incrementing the width of convolution kernel. It's due to the fact that incrementing FOG actually multiplies the computational burden, because

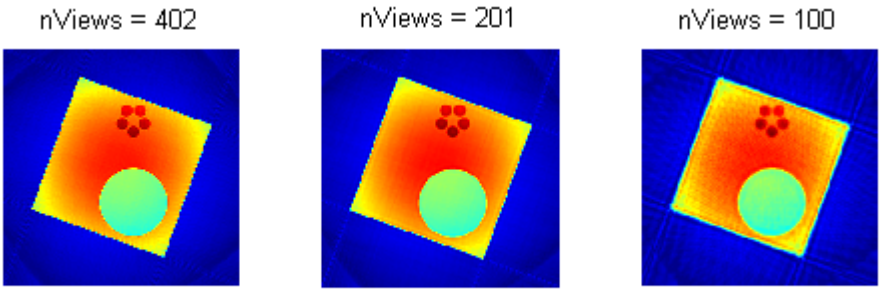

Figure 7.11: Images reconstructed from data acquired with polar undersampling factor of 1,2,3 (left to right).

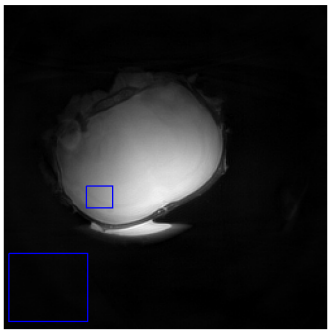

Figure 7.12: Areas of image used for computing of SNR.

there's simply more data to process. Whereas with widening of the kernel, there is only addition of a certain periphery to process within each cycle. The SNR doesn't seem to be an appropriate factor for optimizing the width of the kernel, since up from some value it introduces significant artifact (discussed in chapter 7.2) in the image and down from some value it doesn't takes all grid points into an account in the reconstruction. The remaining range seems to yield rather equivalent SNR. On the other hand the SNR works well in optimization of the FOG, since it clearly proves, that the SNR grows with incrementing FOG. The small descendance around $FOG = 2$ is presumed to be an imperfection of the combination with setting of the width of the kernel. If we were to generalize, then an ideal approach to get optimal results with this particular implementation of gridding would be firts to determine the demand on the SNR, regarding the computation time. Then match the width of kernel to that particular selection of the FOG.

7.5. Testing on spiral data

The spiral phantom was downloaded from [25] in a pack with a gridding software. It doesn't offer original image data, so there only is a possibility to compare results of image reconstruction done by the software from [25] and the software used for reconstruction in

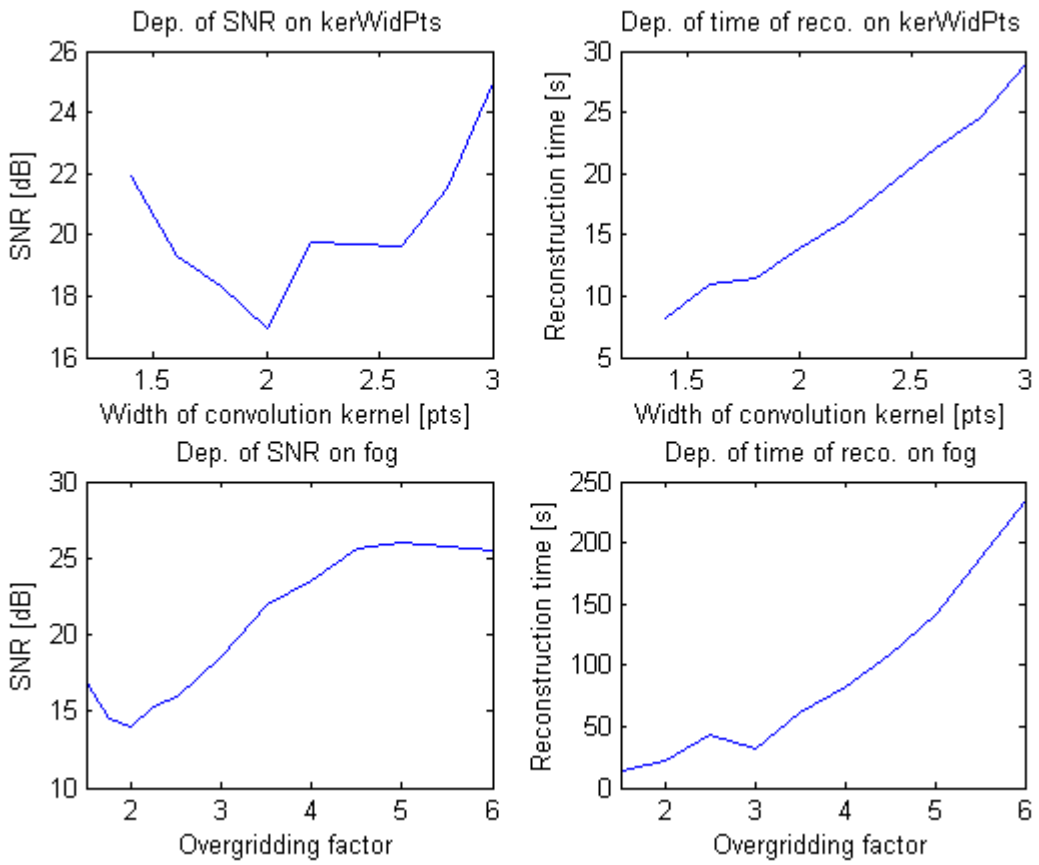

Figure 7.13: Display of results from analysis of SNR and reconstruction time on varying width of convolution kernel and over gridding factor.

this thesis. This chapter is therefore more of an illustrative character, to get the idea of how the software handles the spiral data compared to other more profound implementation of the same reconstruction method.

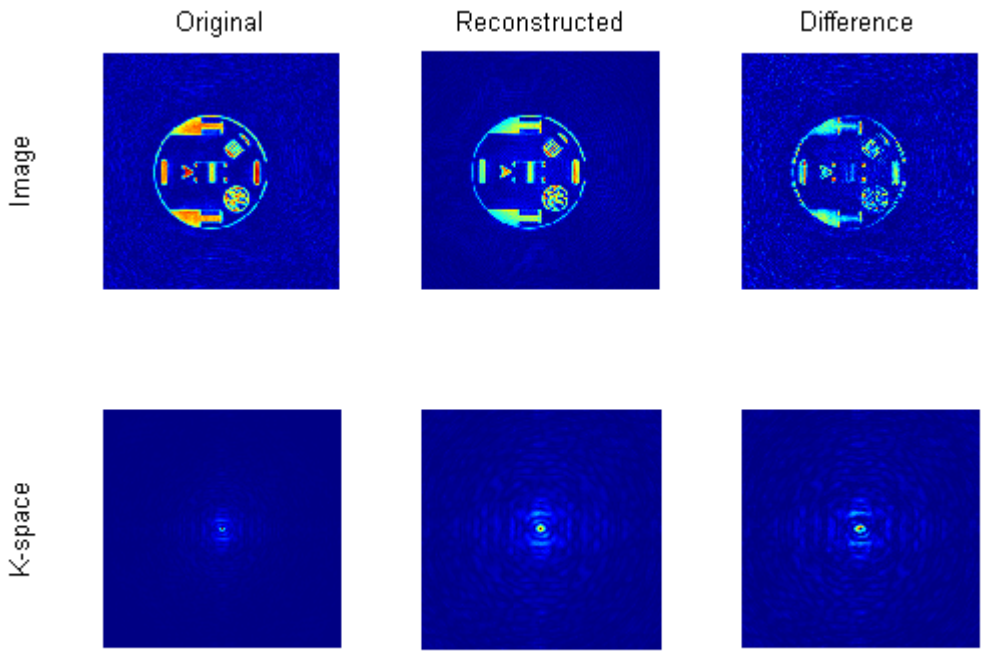

Figure 7.14: Test of reconstruction of data with spiral trajectory. The result of the reconstruction method by Hargreaves *et al* in [25] (left), result of the reconstruction using `gridTP.m` (middle) and the difference image (right).

8. Measurement

Measurements took place on pre-clinical MR systems in the ISI, the MR SOLUTIONS (SMIS) 4.7 T MR system and the Bruker 9.4 T MR system. They were caried out using 2 phantoms, model animals (Rattus norvegicus) and isolated brain of Rattus norvegicus (rat). First phantom consists of two eppendorf tubes (TTP phantom) filled with $2g/l\,H_2O$ solution of $CuSO4$. Second one consists of lockable plastic container filled with plastic beads (PBP phantom), and the same solution as used in TTP. Isolated brain was measured in fomblin.

8.1. MR SOLUTIONS (SMIS) 4.7 T MR system

The MR SOLUTIONS MR system is the older one of the two MR system, the ISI possesses. The installation of this system is somewhat non compact. Some of routine procedures such as a wobbling, or a gradient waveform displaying is done by a third party hardware. The operating software doesn't offer much of the functionality considered standard nowadays. Most significant lack for this thesis turned out to be the absence of an automatic setup protocols. A great part of calibration (described bellow) had to be done manually, which was, on the first touch, rather time consuming and sometimes it could have possibly lead to a non ideal precision of measurement.

Before the measurement, several steps need to be performed in order to set up the system i.e. tuning of the probe, shimming to compensate for B_0 inhomogeneities, offset, etc. Pulse sequences used by MRS are written in c-like language, they have the extension

Figure 8.1: Phantoms used for measurement. The TTP phantom (left), the PBP phantom (middle), and the isolated rat brain in cranium (right).

.ppl. Before such a sequence is used, it must be compiled. During compilation, $.fth$ file is created and, unless the sequence undergoes some change, it doesn't have to be compiled again.

The *.ppl* file, however, doesn't store frequently varying variables i.e. TR, TE, tilt angle. This kind of variables is stored in *.ppr* file. The *.ppr* file further carries the information about geometry and the path to *.ppl* file used. Data display and reconstruction is usually provided by MAREVISI, an image reconstruction, display and analysis software developed by ISI.

The sequence for UTE MRI was taken over from older diploma student in multiple versions, it includes radial k-space sampling, half pulse excitation and on-ramp acquisition. Unfortunately the development of these versions isn't really well documented and non of the versions seems to be fully functional. The shortest reported TE is $250\mu s$ with on-ramp acquisition, however the on-ramp acquisition doesn't seem to be precise enough. Without on-ramp acquisition the shortest reported TE is $500\mu s$. The MRS system doesn't export k-trajectories, so that they have to be calculated using knowledge about gradients, which can introduce errors to reconstruction.

8.1.1. Phantom measurements

Although in time scale 4.7 T MR system measurements were of greater extent, than 9.4 T MR system measurements. The UTE pulse sequence was problematic to debug, since the system doesn't offer much of an insight. Besides the sequence didn't offer echo time short enough. Hence the tendency was to focus more on 9.4 T system as explained at the end of this chapter. On the other hand though hours of measurements and imperfect reconstruction of data with this system, brought a lot of experience with UTE measurement. All the measurements discussed in this chapter were performed with volume receive/transmit coil.

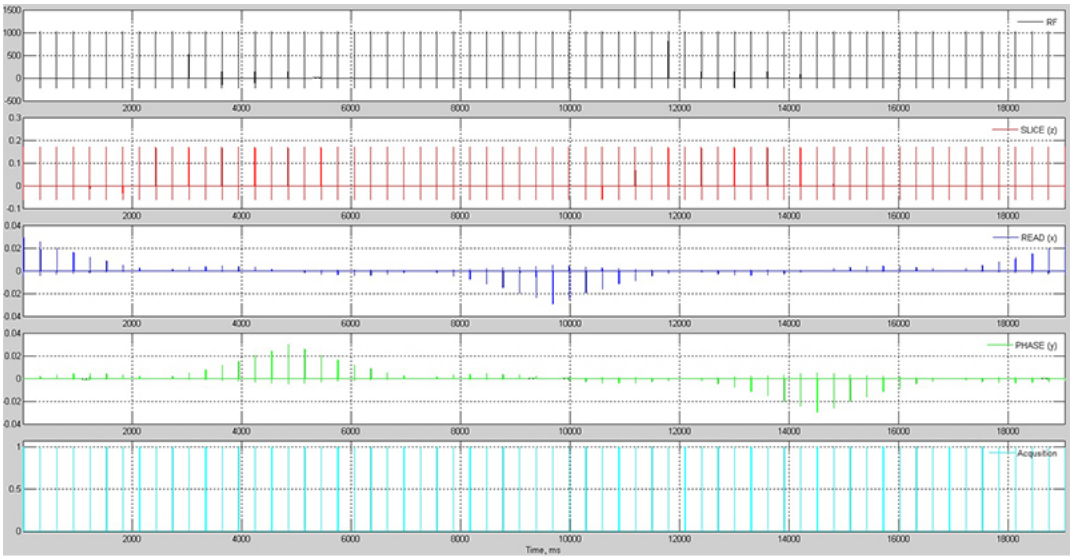

Figure 8.2: Simulation of UTE sequence.

Figure 8.3 shows the PBP acquired without on-ramp acquisition and a subsequent sinogram yielded by series of 1D FFT in readout direction. It only consists of 120 projections with 200 data sample each. This data set was rather than for testing of reconstruction, acquired for illustrative purpose. In the sinogram, we can see thick, white horizontal stripes, most likely introduced by inaccurate system adjustment.

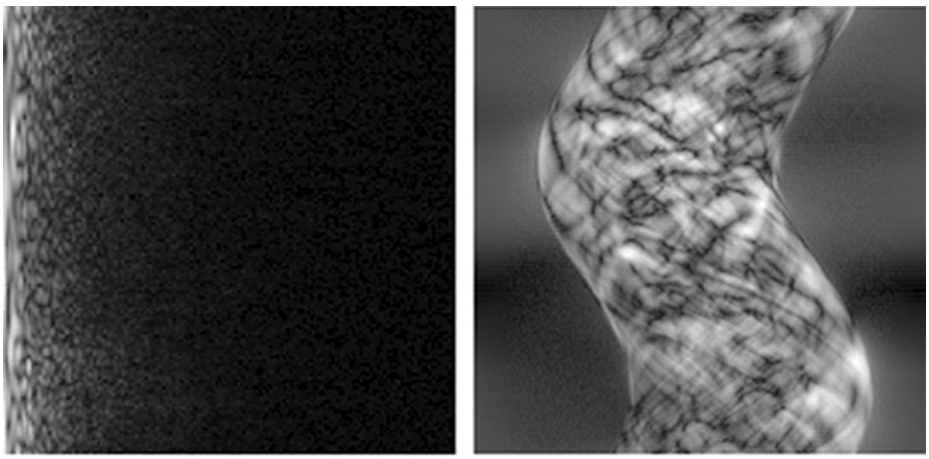

Figure 8.3: PBP acquired in half echo mode with on-ramp acquisition. 120 measured k-space projections with angle going from 0 to 2π (left). Reconstructed sinogram (right).

Figure 8.4 shows the PBP acquired with on-ramp acquisition, however, with on-ramp acquisition, the initial points are not sampled equidistantly, thus FFT is not corect method for reconstruction. To be able to make corect sinogram, series of 1D DFT with computed trajectories should have been exploited. However the echo seems to be shifted from the center of k-space. To be able to diagnose other problems with this sequence, this one was temporarily eliminated by not using on-ramp acquisition.

Following example was carried out with TTP, because of it's more homogenous cross-section. In the figure 8.5 you can see k-space data and subsequent sinogram. It was meant

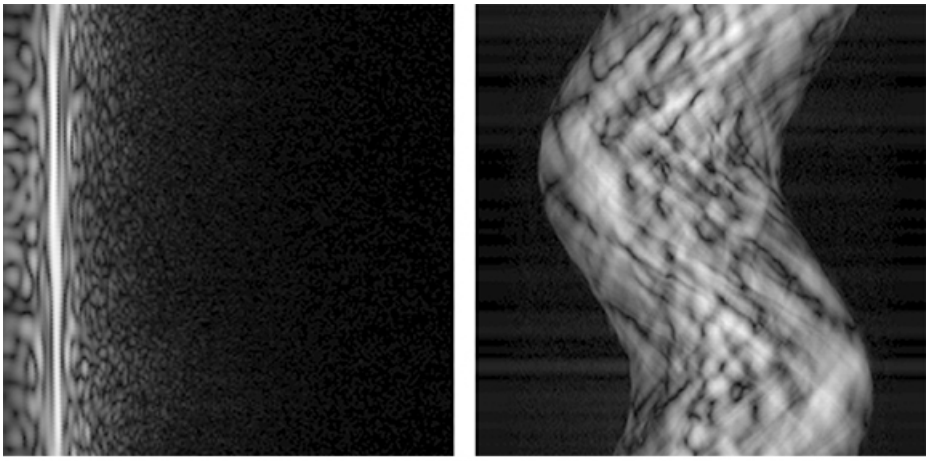

Figure 8.4: PBP acquired in half echo mode with on-ramp acquisition. 120 measured k-space projections with angle going from 0 to 2π (left). Reconstructed sinogram (right).

to form 256px to 256px image, so that 402 projections was measured each containing 128 data points.

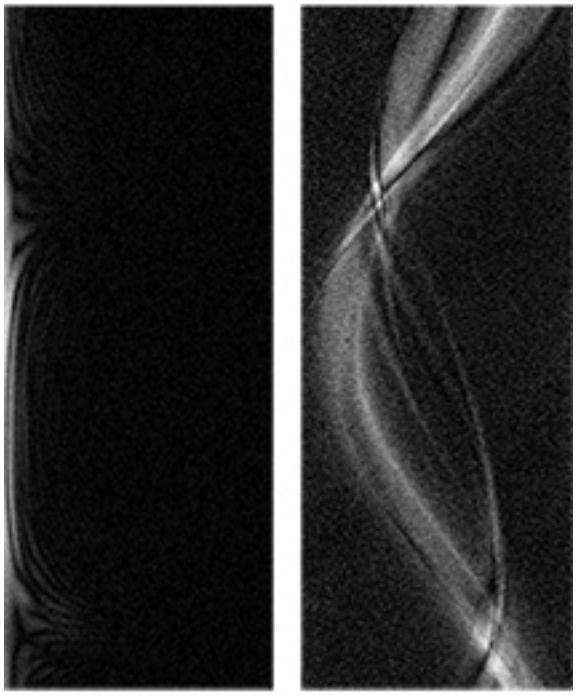

Figure 8.5: TTP acquired in half echo mode without on-ramp acquisition. 402 measured k-space projections with angle going from 0 to 2π (left). Reconstructed sinogram (right).

Reconstruction didn't yield a reasonable image using standard reconstruction parameters, nor with the FOG of 4 as you can see in figure 8.6. in chapter 4.

Extensive amount of time was spend on diagnosing imperfections and causes of foiled reconstructions, wherelse measurements of the 9.4 T system were going smooth. So there was either a possibility to try in praxis the gradient fidelity methods described in chapter 4 to upgrade UTE sequence on 4.7 T system, or to continue with measurements on 9.4 T

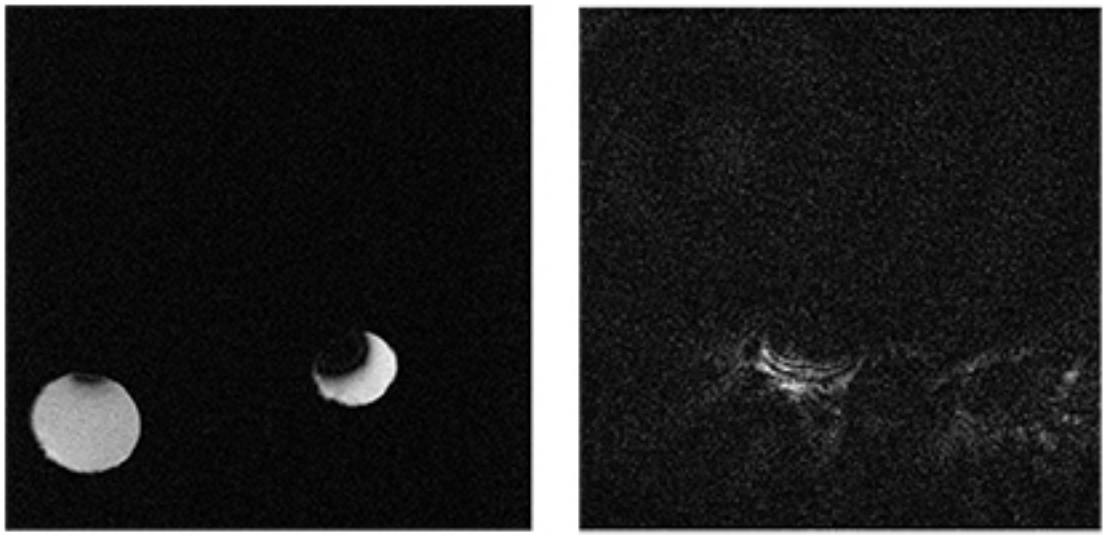

Figure 8.6: Image obtained with GE tripilot (left), image obtained by gridding of data shown in figure 8.4 (right).

system. Second possibility was accepted as more reasonable for several reasons. The measurements of gradient fidelity requires a non-standard pulse sequence which would have to be programmed and debugged as well. The 9.4 T system offers favourable condition for a testing of the reconstruction of both radial and spiral trajectory data. There was a demand to do some pilot UTE studies on 9.4 T system.

8.2. Bruker 9.4 T MR system

The Bruker 9.4 T MR system was installed in 2012. It's rather compact system providing a high level of automation, user comfort and insight into the process of data acquisition, which turned out to be rather useful in case of this thesis. The pulse sequences are written in c language, part of the sequence is an automatic setup sequence, which saves considerable amount of time and trouble. On the other hand this system is being much more occupied. There are two versions of main interface software the ParaVision 5.1 and the ParaVision 6.0, the data output of both versions is of the same format. PV 6.0 is somewhat less reliable. It is conventional in the ISI to perform control measurement with PV 5.1 when exploiting new method with PV 6.0. The advantage of PV 6.0 is implementation of some more advanced methods.

8.2.1. Multi Channel reconstruction

Measurements with 9.4 T system are carried out, using surface receive array coil with four receive channels and volume excitation coil, so that 4 datasets are obtained. The manner of treating this format of data is discutable in some aspects. Bernstein *et al* [5] proposes both simple and advanced methods of channel combinations. After a discussion with the supervisor of this thesis the, in his words, somewhat naive, but not entirely wrong,

summation of absolute values of images reconstructed from each channel, was chosen. It's because in case of treating complex data, a great attention has to be paid to phase of the data, greater than this thesis can cover by it's extent.

8.2.2. UTE sequence

All acquisition acceleration parameters mentioned in chapter 5 are implemented in the pulse sequence for UTE in both PV 5.1 and PV 6.0 (figure 8.7). It is avalible to acquire half projections in FID mode, or whole projections in ECHO mode. Among parameters of the sequence is an automatic minimalizetion of TE. In case of exploiting half RF pulse for excitation, the acquisition of each projection is performed twice, with a negative and a positive slice selection gradient. In such case TE is the minimal possible (tens of μs) is achivable, but the total acquisition time doubles. In case of a time crunch, this could be compensated by acquisition with polar undersampling of 2, which can provide reliable image as shown in chapter 7.3 for phantom data, and later in this chapter for real data. Very important difference between UTE sequences in PV 5.1 and PV 6.0 is the fact, that PV 5.1 doesn't allow deactivate TE minimalization in FID mode, which makes user unable to perform scans with different echo times, PV 6.0 allows this deactivation and thus chosing of TE in FID mode. Another important thing is, that this sequence doesn't offer any way of suppressing long T_2 components. So when there was demand for example myelin imaging, alternative approaches had to be considered.

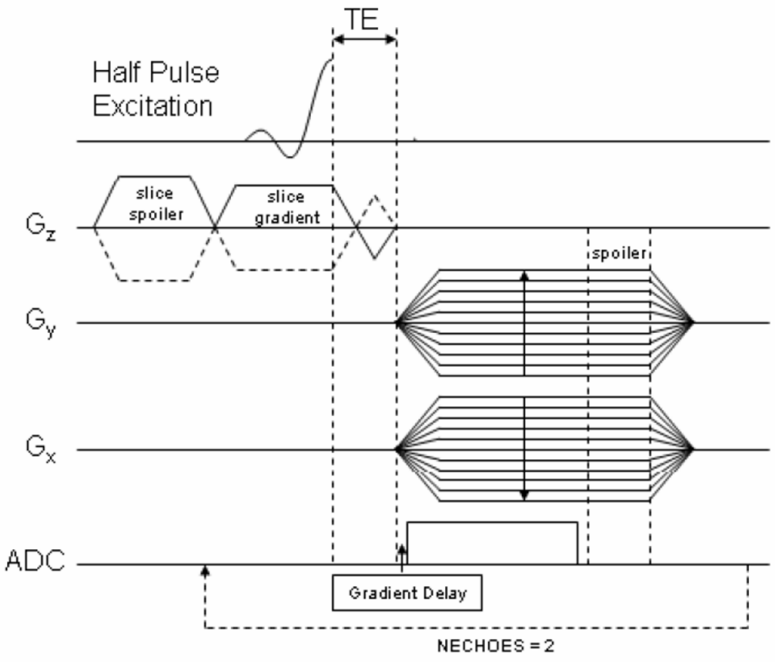

Figure 8.7: UTE pulse sequence diagram taken from the official Bruker Ltd. PV 6.0 manual. This sequence is able to achive echo time in tens of μs.

8.2.3. SPIRAL sequence

Spiral pulse sequence implemented in the 9.4 T system appears to be rather advanced. Unfortunately, after performing set of pilot scans, it was figured out, that the data output and trajectory output mismatch in dimensions. There is simply more data points,than trajectory points. Solution to this problem wasn't found before the end of works on this thesis, but it is to be solved in future progress.

8.2.4. Phantom measurments

Measurements discussed in this section were carried on the PBP using rat receive surface array coil. No interpolation error was introduced to this data so we can eliminate the e_{inter} factor from eq. 7.2, thus it might be possible to reconstruct these data using more favorable parameters. In the figure 8.8 reconstruction with various parameters is preformed and it is clear enough, that it is possible to reconstruct a reliable image with the overgridding factor of 1.5, such value is comparable to those to be found in literature. Please note, that the intensity gradient in all the figures is a result of imaging using surface coil.

In the figure 8.9 on the left, resulting image is shown. In the middle there is zoomed (10000x) center of the k-space, interesting thing is, that there is no trully central point, sampling starts with certain offset from the center of k-space. On the left you can see central part of k-space please note the variable distance between 2 circles of data samples, that is related to on-ramp acquisition.

In the figure 8.10 you can see the difference between images reconstructed from datasets with different polar undersampling. It is againg shown, that even with polar undersampling factor of 2, reliable image can be reconstructed.

8.2.5. Animal model measurments

During a Parkinson's disease study in the ISI, an opportunity appeared to perform a UTE measurement on animal models. Model animals were rats (Rattus norvegicus) with untreated Parkinson's disease and healthy controls. One of secondary demands was to get the idea about possibilities of imaging myelin on 9.4 T system using UTE. And since UTE is not commonly used in the ISI, there was a need to make a several pilot measurments, to determine current state of matters.

As already stated, it is favorable to suppress long T_2 components, so it doesn't overcome the short T_2 components' signal. However the UTE sequence implemented by manufacturer doesn't offer the possibility to include an inversion pulse to the sequence. Anyway, there is a possibility to acquire data with different TE in range from the shortest TE achivable, to TE leaving the longest T_2 components only and then perform and interpret the subtractions.

Application of this method can be seen in figures 8.13 and 8.12. You can see minimum echo time images in the first rows. The left columns then represent reconstructed images of later echoes and right columns their subtractions from the TE_{min} image (figure 8.11). However the data in the figure 8.12 is measured in the PV 5.1, so that the first image are acquired in FID mode and all the others in ECHO mode, which allows variation of TE, thus it can't be used for interpretation. Besides images reconstructed from data measured

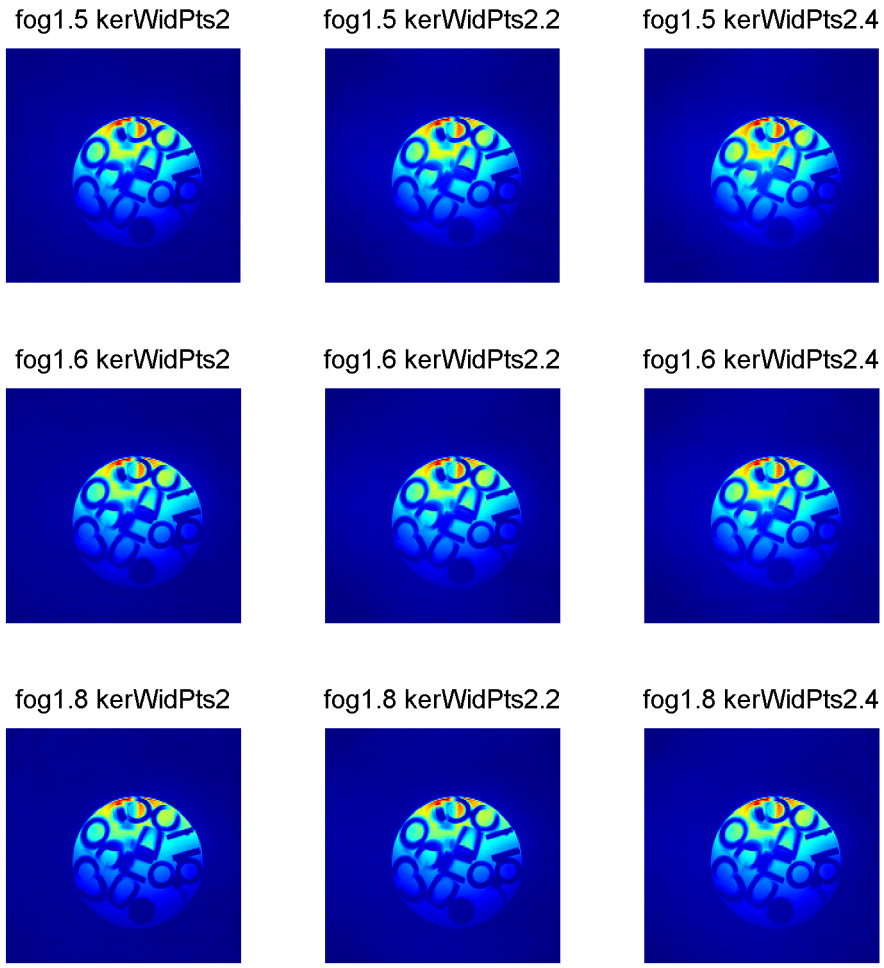

Figure 8.8: Reconstruction for varying reconstruction parameters.

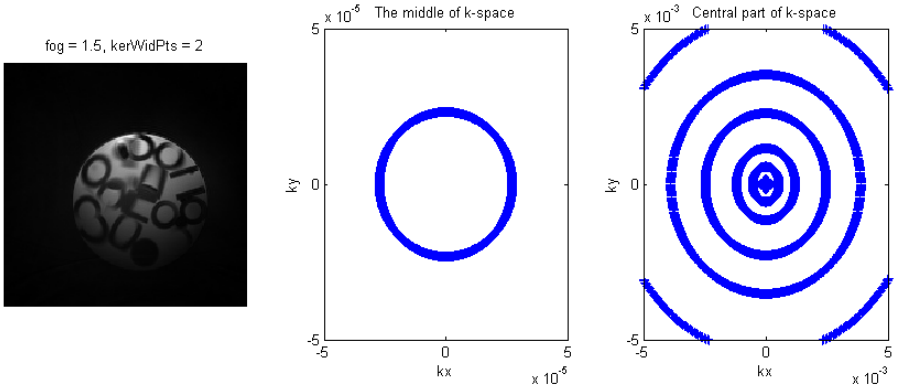

Figure 8.9: Grayscale image (left), zoom into centre of k-trajectories (middle), zoom into central area of k-trajectories (right).

in ECHO mode posses some sort of shift artefact, most likely similar to EPI artifacts, which is possible due to similar trajectory.

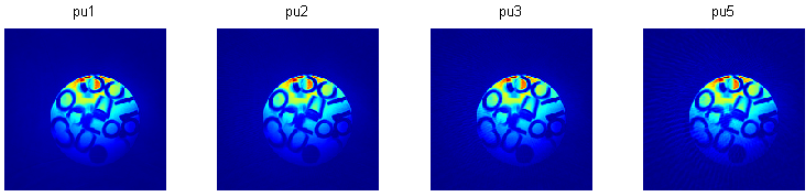

Figure 8.10: Reconstruction for varying reconstruction parameters.

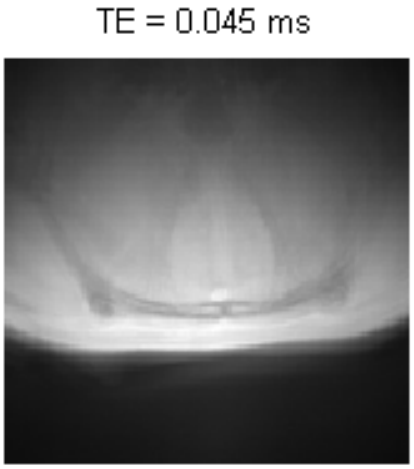

Figure 8.11: Rat brain scanned with minimal possible echo time $45\mu s$. It almost exactly represents H_2 proton density spread, *i.e.* we obtain signal from almost all the tissue from excited slice.

The data shown in the figure 8.13 are measured with PV 6.0, but in this case, data are affected by SSFP artefact (horizontal stripes for example in the image acquired with TE = 5 ms). So they are not reliable as well.

There was not much of a success enhancing myelin signal using subtracting form later echoes. Another manner to determine the state of myelin at least in the region of interest, which is, in this case corpus callosum, has to be proposed. Corpus callosum is a region of brain with a significant content of white matter and thus myelin. There was a presumption that supposing that image of latter echoes fit with the one of TE_{min}.

With certain simplification the tissue within certain area, can be considered to be a composition of tissues with a majority of short T_2 components and tissues with a majority of short T_2 components. In such case the magnetization decay might be considered exponential with one fast decaying component and one slow decaying component. So that a model of this system could be made and the parameters of the decay curves determined. Testing of this approach started with measurement on isolated rat brain. Precautions

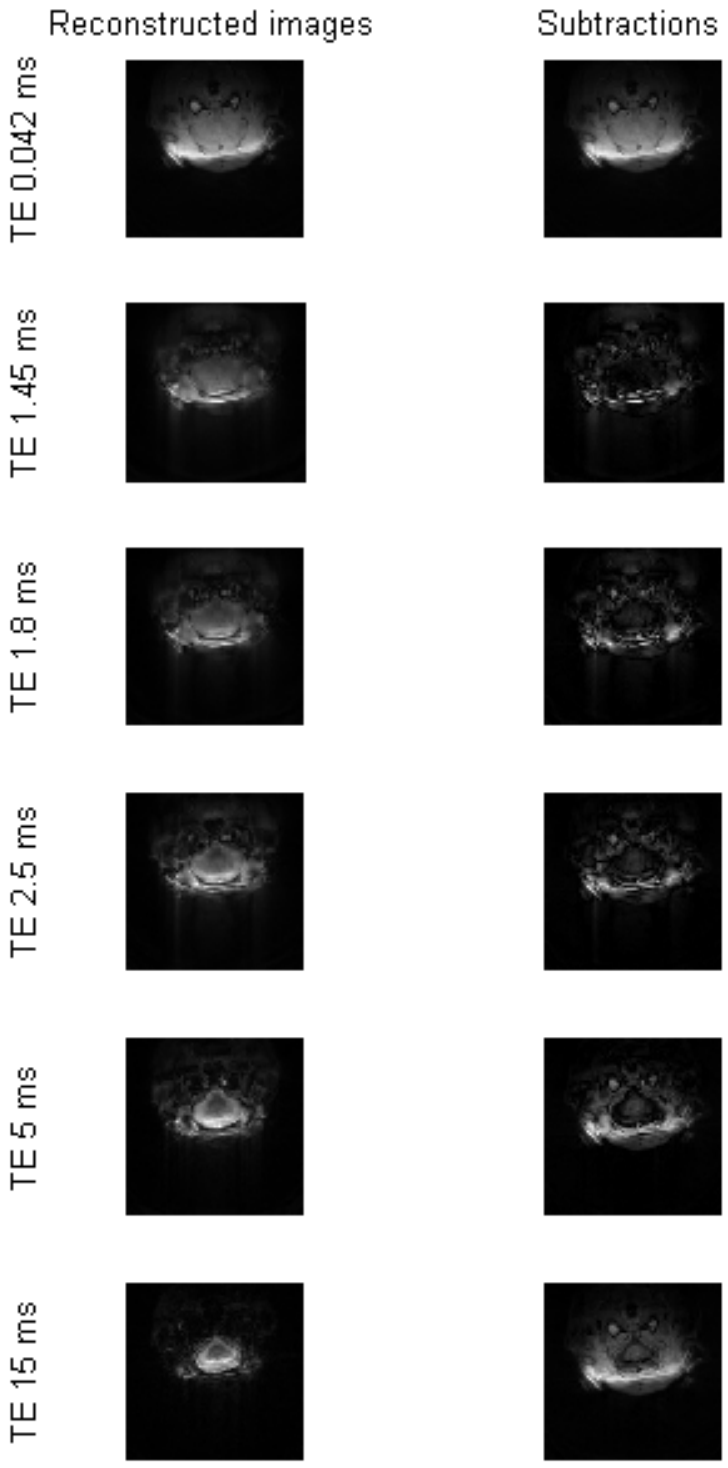

Figure 8.12: Reconstruction for varying reconstruction parameters.

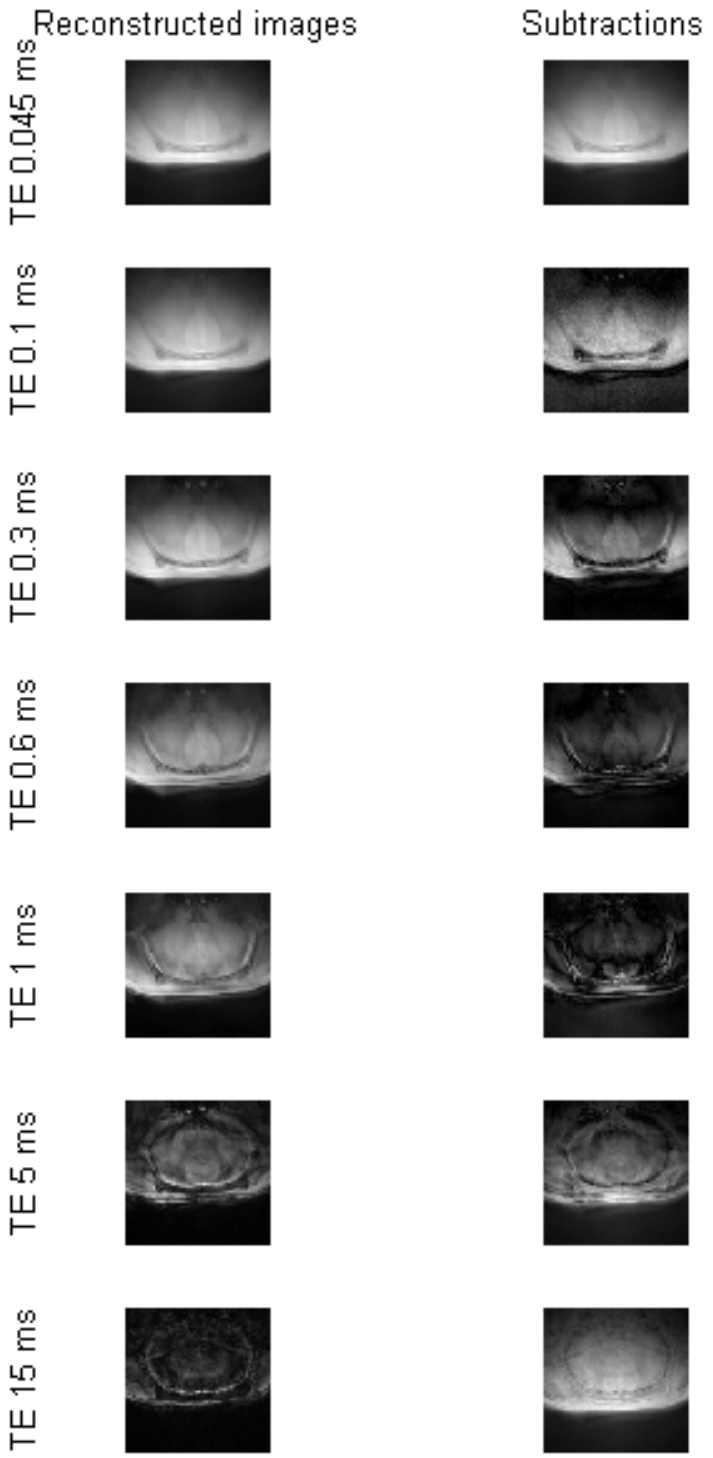

Figure 8.13: Reconstruction for varying reconstruction parameters.

were taken (TR increased) to eliminate SSFP artifacts this time. In the figure 8.14 you can see series of images of UTE images with 12 different echo times, with corpus callosum marked with red arrow. Images seem to be free of artifacts.

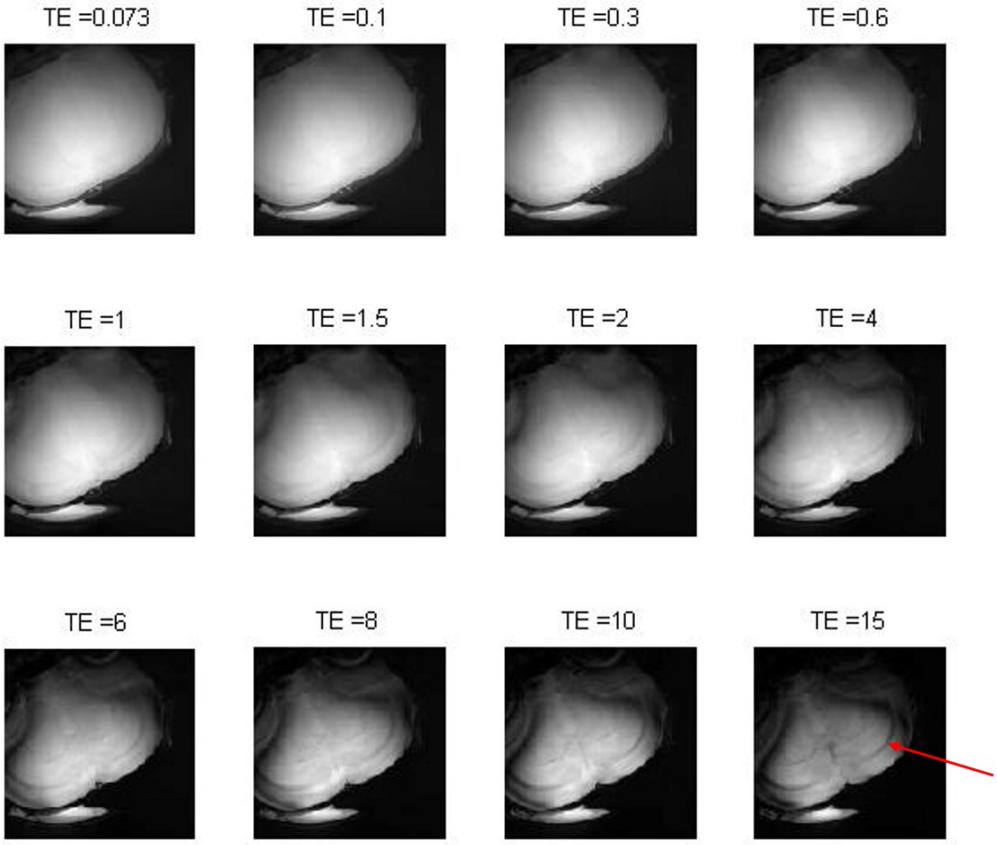

Figure 8.14: UTE of isolated rat brain. Red arrow points to corpus callosum, the area of interest in this case.

In the figure 8.15, decay of signal from different areas, which, again, with on certain level of abstraction, could represent individual kinds of tissue. The upper row is supposed to represent the corpus callosum (heavily myelinated), middle row represents bone, and lower row represents standard white matter. The progressions of the decays approximately meet the expectations, it's rather well visible in the bone example. Next step would be to fit decay curves onto a biexponential model, which is out of scope of this, but it will be done in future progress.

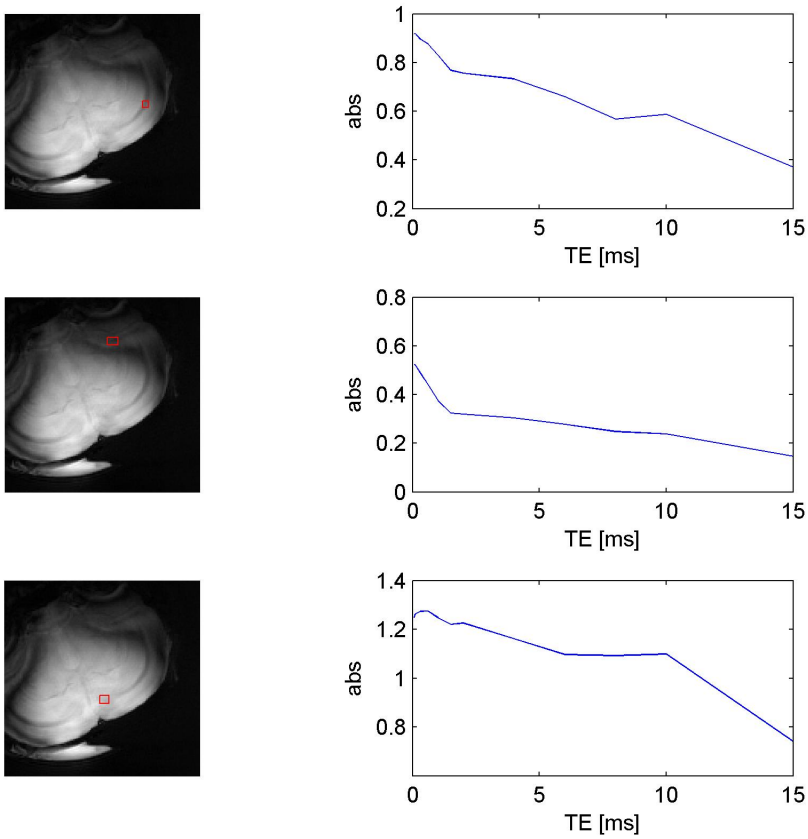

Figure 8.15: Decay of pixel intensity from images in figure 8.14 with growing TE. The value represents summation over red area in the image.

9. Discussion

Theoretical introduction to MRI was intended to be simple, but still exact and cover all the important phenomena. This expectation was not fully met due to it's difficulty and great time demand. Chapter about k-space would be most adequate for this thesis, to support later discussions, but it wasn't completed. I hope, that relatively extensive experimental progress will partly compensate for it.

Reconstruction methods were widely discussed in this thesis, as well as during my summer internship in the ISI, so I believe, that the decision to exploit gridding is rather solid. The implementation of gridding meets expectations regarding quality of reconstruction and software realization. Several mechanisms are added were implemented to make the reconstruction as fast as possible, but still it is slow compared to, for example, software available online [25], which is on the other hand written in c. Further progress will probably lead to transformation to c-language, for computing acceleration.

Gradient fidelity measurements were discussed, but not performed experimentally, due to a slight turn in preferences and sudden relative decrease of its necessity. It was decided to continue measurements at the 9.4 system, which is in a good state and no significant gradient infidelities are expected.

Animal model measurement performed, were ones of the first UTE studies with 9.4 T system, with minimum prior knowledge about pulse sequence and subsequent reconstruction behavior. I belive, that this thesis provides a certain clerifications and experiences, which will be applicable for future studies.

Conclusion

This thesis was intended to deal with image reconstruction from non-cartesian MRI data, and fast MRI imaging techniques with a focus on UTE.

Image reconstruction was discussed and the gridding method was chosen to be tested and implemented. The results of the implementation are good in terms of quality. In terms of reconstruction time, there is still a reserve. Reconstruction was used to reconstruct real data from 2 MR systems of the ISI. In case of 4.7 MR SOLUTIONS system, the reconstruction was unsuccessful due to pulse sequence imperfections. Radial data from the 9.4 T Bruker MR systems were reconstructed without any probles. Spiral data from the same system were impossible to reconstruct due to unexpected format of the data.

Measurement with UTE pulse sequence were performed on phantoms, isolated rat brain and animal models. The experimental part continued with myelin imaging.

Bibliography

[1] GEVA, Tal. Magnetic Resonance Imaging: Historical Perspective. *Journal of Cardiovascular Magnetic Resonance.*2006, vol. 8, issue 4, s. 573-580. DOI: 10.1080/10976640600755302.

[2] BECKER, Edwin D. A BRIEF HISTORY OF NUCLEAR MAGNETIC RESONANCE. *Analytical Chemistry.* 1993, vol. 65, issue 6, 295A-302A. DOI: 10.1021/ac00054a716.

[3] (AT LEAST SOME) HISTORY OF THE NMR. *University of Oulu, NMR laboratory* [online]. 2013 [cit. 2015-01-04]. Dostupné z: http://www.oulu.fi/nmrlab/nmrhistory.html

[4] LEVITT, Malcolm H. *Spin dynamics: basics of nuclear magnetic resonance.* New York: John Wiley, 2001, xxiv, 686 p. ISBN 04-714-8922-0.

[5] BERNSTEIN, Matt A, Kevin Franklin KING a Ziaohong Joe ZHOU.*Handbook of MRI pulse sequences.*. Boston: Academic Press, c2004, xxii,1017 p. ISBN 01-209-2861-2.

[6] HAACKE, E.*Magnetic resonance imaging: physical principles and sequence design.*. New York: Wiley, c1999, xxvii, 914 p. ISBN 04-713-5128-8.

[7] LIU, Hui a Gerald MATSON. Accurate Measurement of Magnetic Resonance Imaging Gradient Characteristics. *Materials* [online]. 2014, vol. 7, issue 1, s. 1-15 [cit. 2014-12-28]. DOI: 10.3390/ma7010001. Dostupné z: http://www.mdpi.com/1996-1944/7/1/1/

[8] LATTA, Peter, Marco L.H. GRUWEL, Vyacheslav VOLOTOVSKYY, Michael H. WEBER a Boguslaw TOMANEK. Simple phase method for measurement of magnetic field gradient waveforms. *Magnetic Resonance Imaging* [online]. 2007, vol. 25, issue 9, s. 1272-1276 [cit. 2014-12-29]. DOI: 10.1016/j.mri.2007.02.002.

[9] YANG, Zhili a Mathews JACOB. Mean square optimal NUFFT approximation for efficient non-Cartesian MRI reconstruction. *Journal of Magnetic Resonance.* 2014, vol. 242, s. 126-135. DOI: 10.1016/j.jmr.2014.01.016.

[10] O'SULLIVAN, J. D. A Fast Sinc Function Gridding Algorithm for Fourier Inversion in Computer Tomography. *IEEE Transactions on Medical Imaging.* 1985, vol. 4, issue 4, s. 200-207. DOI: 10.1109/tmi.1985.4307723.

[11] FTWAW Wajer, Non-Cartesian MRI Scan Time Reduction through Sparse Sampling, PhD Thesis, Technische Universiteit Delft, 2001

[12] DALE, B., M. WENDT a J.L. DUERK. A rapid look-up table method for reconstructing MR images from arbitrary K-space trajectories. *IEEE Transactions on Medical Imaging.* 2001, vol. 20, issue 3, s. 207-217. DOI: 10.1109/42.918471.

[13] JACKSON, J.I., C.H. MEYER, D.G. NISHIMURA a A. MACOVSKI. Selection of a convolution function for Fourier inversion using gridding (computerised tomography application). *IEEE Transactions on Medical Imaging.* 1991, vol. 10, issue 3, s. 473-478. DOI: 10.1109/42.97598.

[14] DUTT, A. a V. ROKHLIN. Fast Fourier Transforms for Nonequispaced Data. *SIAM Journal on Scientific Computing.* 1993, vol. 14, issue 6, s. 1368-1393. DOI: 10.1137/0914081.

[15] YANG, Zhili a Mathews JACOB. Efficient NUFFT algorithm for non-Cartesian MRI reconstruction. *2009 IEEE International Symposium on Biomedical Imaging: From Nano to Macro.* 2009. DOI: 10.1109/isbi.2009.5192997.

[16] TYLER, Damian J., Matthew D. ROBSON, R. Mark HENKELMAN, Ian R. YOUNG a Graeme M. BYDDER. 2007. Magnetic resonance imaging with ultrashort TE (UTE) PULSE sequences: Technical considerations. *Journal of Magnetic Resonance Imaging.* 25(2): 279-289. DOI: 10.1002/jmri.20851.

[17] ROBSON, Matthew D., Peter D. GATEHOUSE, Mark BYDDER a Graeme M. BYDDER. Magnetic Resonance: An Introduction to Ultrashort TE (UTE) Imaging. *Journal of Computer Assisted Tomography.* 2003, 27(6): 825-846. DOI: 10.1097/00004728-200311000-00001.

[18] LARSON, Peder E. Z., Steven M. CONOLLY, John M. PAULY a Dwight G. NISHIMURA. Using adiabatic inversion pulses for long-T2 suppression in ultrashort echo time (UTE) imaging. *Magnetic Resonance in Medicine.* 2007, 58(5): 952-961. DOI: 10.1002/mrm.21341.

[19] ROBSON, Matthew D. a Graeme M. BYDDER. Clinical ultrashort echo time imaging of bone and other connective tissues. *NMR in Biomedicine.* 2006, 19(7): 765-780. DOI: 10.1002/nbm.1100.

[20] WILHELM, M. J., H. H. ONG, S. L. WEHRLI, C. LI, P.-H. TSAI, D. B. HACKNEY, F. W. WEHRLI, Jacob VALK, Marjo S. van der KNAAP, et al. Direct magnetic resonance detection of myelin and prospects for quantitative imaging of myelin density. *Proceedings of the National Academy of Sciences.* 2012, 109(24): 445-456. DOI: 10.1007/978-3-662-03078-3-71.

[21] BERGIN, C J, J M PAULY a A MACOVSKI. Lung parenchyma: projection reconstruction MR imaging. *Radiology.* 1991, 179(3): 777-781. DOI: 10.1117/1.3275472.2.

[22] MANSFIELD, P. Multi-planar image formation using NMR spin echoes. *Journal of Physics C: Solid State Physics.* 1977, 10(3): L55-L58. DOI: 10.1088/0022-3719/10/3/004.

[23] AHN, C. B., J. H. KIM a Z. H. CHO. High-Speed Spiral-Scan Echo Planar NMR Imaging-I. *IEEE Transactions on Medical Imaging.* 1986, 5(1): 2-7. DOI: 10.1109/tmi.1986.4307732.

[24] BEATTY, P.J., D.G. NISHIMURA a J.M. PAULY. Rapid gridding reconstruction with a minimal oversampling ratio. *IEEE Transactions on Medical Imaging.* 2005, 24(6): 245-248. DOI: 10.1109/9780470545461.ch28.

[25] Gridding Functions. HARGREAVES, Brian a Philip BEATTY. *MRSRL: Magnetic Resonance Systems Research Laboratory* [online]. 2004 [cit. 2015-05-24]. Dostupné z: http://mrsrl.stanford.edu/ brian/gridding/

List of used abbreviations and symbols

DCF	Density compensation function
DFT	Discrete Fourier transform
DTI	Diffusion tensor imaging
EPI	Echo-planar imaging
FFT	Fast Fourier transform
FID	Free induction decay
FOV	Field of view
fMRI	Functional magnetic resonance imaging
GE	Gradient echo
GIRF	Gradient impulse response function
IDFT	Inverse discrete Fourier transform
IFFT	Inverse fast Fourier transform
ISI	Institute of Scientific Instruments of the ASCR, v. v. i.
KB	Kaiser-Bessel
LUT	Lookup table
MRI	Magnetic resonance imaging
MRS	MR SOLUTIONS Ltd.
NUFFT	Non-uniform fast Fourier transform
NMR	Nuclear magnetic resonance
PBP	Plastic beads phantom
PV	ParaVision
RF	Radio frequency
SEPI	Spiral echo planar imaging
SNR	Signal to noise ratio
SW	Software
TE	Time to echo

TR	Repetition time
TTP	Two tubes phantom
UTE	Ultra short echo time

List of annexes

- Functions
  - *bru2mat.m*
  - *gridTP.m*
  - *mrd2mat.m*
  - *radLoc.m*
  - *traj2mat.m*
  - *radLoc.m*
  - *readme.doc*
- Examples
  - Phantom
    - Radial
    - Spiral
  - 94
  - 47